A unique ternary Ce(III)-quercetin-phenanthroline assembly with antioxidant and anti-inflammatory properties.

E. Halevas,[a,b] S. Matsia,[a] A. Hatzidimitriou,[c] E. Geromichalou,[d] G. Geromichalos[c,e], T. A. Papadopoulos,[f] G. Katsipis,[e] A. Pantazaki,[e] G. Litsardakis,[b] A. Salifoglou[a*]

[*] Authors to whom correspondence should be addressed.
Tel: +30-2310-996-179 Fax: +30-2310-996-196 E-mail: salif@auth.gr
Tel: +30-2310-996-384 Fax: +30-2310-996-302 E-mail: lefterishalevas@gmail.com

[a] Laboratory of Inorganic Chemistry, Department of Chemical Engineering, Aristotle University of Thessaloniki, Thessaloniki 54124, Greece

[b] Laboratory of Materials for Electrotechnics, Department of Electrical and Computer Engineering, Aristotle University of Thessaloniki, Thessaloniki 54124, Greece

[c] Laboratory of Inorganic Chemistry, Department of Chemistry, Aristotle University of Thessaloniki, Thessaloniki 54124, Greece

[d] Laboratory of Pharmacology, Medical School, National and Kapodistrian University of Athens, Athens 11527, Greece

[e] Laboratory of Biochemistry, Department of Chemistry, Aristotle University of Thessaloniki, Thessaloniki 54124, Greece

[f] Faculty of Science and Engineering, Thornton Science Park, University of Chester, CH2 4NU, Chester, U.K.

Abstract

Quercetin is one of the most bioactive and common dietary flavonoids, with a significant repertoire of biological and pharmacological properties. The biological activity of quercetin, however, is influenced by its limited solubility and bioavailability, thereby necessitating new ways of achieving optimal tissue cellular absorbability. To that end, metal ion complexation offers a significant option, with lanthanide cerium known for its protective effects in neurological disorders, cell radiation, and carcinogenicity. Driven by the need to optimally enhance quercetin bioavailability and bioactivity through complexation, synthetic efforts led to the isolation of a ternary Ce(III)-quercetin-(1,10-phenanthroline) (**1**) compound. Physicochemical characterization (elemental analysis, FT-IR, Thermogravimetric analysis (TGA), UV-Visible, NMR, Electron Spray Ionization-Mass Spectrometry, Fluorescence, X-rays) revealed its solid-state and solution properties, with significant information emanating from the coordination sphere composition of Ce(III), encompassing singly deprotonated quercetin, the aromatic chelator 1,10-phenanthroline and bound nitrato ligands. The experimental data justified further entry of **1** to biological studies involving toxicity, ROS-suppressing potential, cell metabolism inhibition in cultures of *S. cerevisiae*, and plasmid DNA degradation. *In silico* studies showed binding of **1** to DNA, DNA gyrase and glutathione S-transferase, providing useful complementary insight into the elucidation of the mechanism of action of **1** at the molecular level and interpretation of its bio-activity. The collective work projects the importance of physicochemically supported biological activity profile of well-defined Ce(III)-flavonoid compounds, thereby establishing grounds for further focused pursuit of new hybrid metal-organic materials, effectively enhancing the biological role of naturally-occurring flavonoids in physiology and disease administration.

Keywords: Cerium-Quercetin synthesis, complex formation and crystal structure, antibacterial activity, DNA degradation, oxidative stress, *in silico* molecular docking

1. Introduction

Flavonoids represent a group of secondary metabolites based on the 2-phenylchromen-4-one (2-phenyl-1-benzopyran-4-one) core structure. They occur in nature mostly as polyphenol compounds of plant origin [**1**]. Depending on the degree of oxidation of the γ-pyranone ring, they can be categorized into different subclasses, such as flavones, flavonols, and flavanones. In addition to naturally occurring flavonoids, there are also many synthetic flavonoid-derived substances [**2-6]**.

In nature, flavonoids occur mostly as glycosides, with the sugar group enhancing water solubility of the hydrophobic flavonoid molecules. Flavonoids have shown promising antioxidant, anti-virus, anti-inflammatory and anti-cancer activities [**7,8**], with recent studies showing that they can also act as enzyme inhibitors [**9**], signaling molecules [**10,11**], DNA intercalators [**12,13**], and metal-ion chelators [**14**]. Dietary flavonoids exhibit neuroprotective properties, shielding neurons against injury and promoting memory, learning, and cognitive function [**15,16**]**.** In that respect, they serve as a key class of molecules in the development of therapeutics in Alzheimer's disease (AD). Their beneficial properties are ascribed to their ability to scavenge free radicals, an important antioxidant activity, which depends heavily on the number and position of oxo and alcoholic-phenolic moieties as well as nitrogen donors in some synthetic compounds [**17**].

Quercetin (3,5,7,3',4'-pentahydroxyflavone) (QC), is a well-known flavonoid generally found in fruits and vegetables, with extensive nutraceutical and pharmaceutical use [**18**], mainly due to its high oxygen radical scavenging activity or its ability to inhibit xanthine oxidase and lipid peroxidation *in vitro* [**19**]. QC reliably exerts neuroprotective effects against agent-induced toxicity [**20**] and increases the resistance of neurons to oxidative stress and excitotoxicity by modulating mechanisms of cell death [**21,22].** Other studies have shown that it produces an anti-inflammatory effect [**23**], by inhibiting iNOS [**24**], regulating the expression of COX-2 [**25,26**], and exhibiting an anti-proliferative effect on some types of cancer [**27,28**], via mechanisms that activate cell senescence, apoptosis [**29**], and autophagy [**30**]. Moreover, scientific reports have established its ability to penetrate the blood brain barrier [**31,32**], and its protective effect against ischemia [**33**], and atherosclerosis [**34**]. QC has been suggested to exert anti-anxiety and cognitive enhancement, by stimulating or inhibiting enzyme activities/signal transduction pathways [**35**].

With regard to their biological interaction chemistry, flavonoids exhibit more than one possible chelating sites and as polyphenolic compounds they are weak acids undergoing

deprotonation, thereby strongly affecting coordination of metal ions [**36**]. They can bind metal ions in their neutral or anionic form. Metal coordination to QC can occur *via* the 3-hydroxyl and 4-carbonyl group of the C ring, the 4-carbonyl-5-hydroxyl site of the A and C rings or *via* the catechol moiety of the B ring (**Scheme 1**).

Depending on the metal ion, redox reactions between metal ions and ligands may occur, as most flavonoids have good reducing capacity. This is particularly relevant to metal ions with oxidizing properties, such as Fe(III) [**37**], Ru(III) [**38**], Ru(IV) [**39**], Au(III) [**40**], or Os(VIII) [**41**]. The preferred binding site depends on the flavonoid, metal ion and solution pH value. A large number of experimental and theoretical studies on the coordination properties of flavonoids have been reported with contradictory results on the binding site and metal/ligand stoichiometry which, however, is due to the variation of experimental conditions in the different studies conducted [**42-46**]**.**

The number of structurally characterized metal flavonoid complexes is rather limited. So far, the X-ray structures of 3-hydroxyflavone with Cu(I) [**47,48**]**,** Cu(II) [**49,50**], and Fe(II) [**51**], morin-5-sulfonic acid with Zn(II) [**52**], and 4'-methoxyflavonol with Fe(III) are known [53], whereas structures of ternary flavonoid complexes containing additional mono-, di-, tri- or tetradentate *N*- or *N,O* donor ligands are somewhat more abundant and include flavonol and 4'-methoxyflavonol complexes of Fe(II) [**54**], Fe(III) [**55,56**]**,** Cu(II) [**57-64**]**,** Co(II) [**54,57,65,66**]**,** Mn(II) [**53,56,57**]**,** Zn(II) [**57,67**], and Ni(II) [**54,57,68**], and the oxido-bridged Fe(III) complex with *N,N*-bis(6-phenyl-2-pyridyl)methyl)-*N*-((2-pyridyl)methylamine) [57]. The aim of the synthesis of these complexes was to model the enzyme-substrate complex of quercetin 2,3-dioxygenase in the oxidative degradation of QC to the depside [**69**]. Nevertheless, no rare earth flavonoid complexes have been reported in the literature.

Poised to investigate the design of molecular flavonoid compounds, a) combining the overall effects of such organic ligands and metals in their complex form(s), b) providing enhanced redox, magnetic and/or luminescent properties, together with increased antioxidant and anti-inflammatory activity through metal ion chelation, c) potentially enhancing their solubility, bioavailability, and function through metal ion complexation, and d) introducing new hybrid bio-active materials that can ultimately function as building blocks of more elaborate structures, we herein introduce a new crystalline ternary complex assembly of Ce(III) with QC and the ancillary aromatic chelator 1,10-phenanthroline (phen), which is to the best of our knowledge the only such system crystallographically characterized with a rare earth as the central metal ion. The structural composition and physicochemical properties of the newly

arisen material prompted further investigation of its biological reactivity profile, encompassing a) toxicity, ROS-suppressing potential determination, cell metabolism inhibition in cultures of *S. cerevisiae*, and plasmid DNA degradation, and b) *in silico* studies pertaining to binding of **1** to DNA, DNA gyrase, and glutathione S-transferase, collectively establishing the molecular basis for its potential use as a hybrid metallopharmaceutical agent.

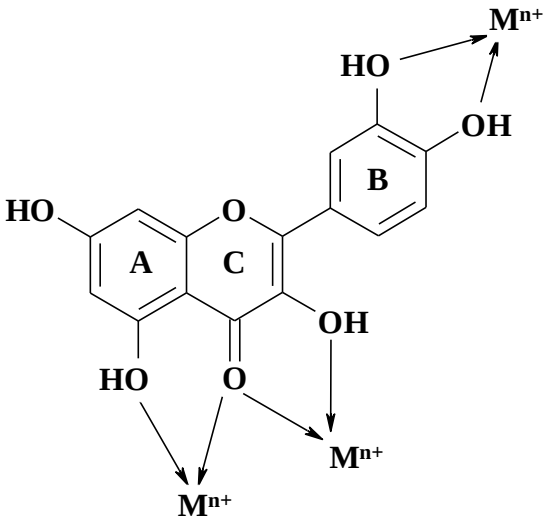

Scheme 1: Potential chelating sites of QC.

2. Experimental Section

2.1. Materials and Methods. All experiments were carried out under aerobic conditions. The structures of the employed ligands are shown in **Scheme 2**. The following starting materials were purchased from commercial sources (Sigma, Fluka) and were used without further purification: quercetin dehydrate (QC), 1,10-phenanthroline (phen), and cerium nitrate hexahydrate ($Ce(NO_3)_3 \cdot 6H_2O$). Solvents: methanol, diethylether. The isolated compound is air-stable at room temperature.

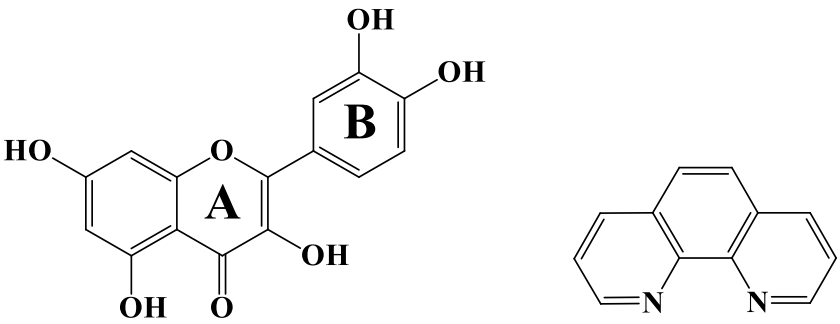

Quercetin **1,10-phenanthroline**

Scheme 2: Schematic representation of the ligands used in this study.

2.1.1. Physical measurements. FT-Infrared spectra were recorded on a Perkin Elmer 1760X FT-infrared spectrometer. A ThermoFinnigan Flash EA 1112 CHNS elemental analyzer was used for the simultaneous determination of carbon, hydrogen, and nitrogen (%). The analyzer operation is based on the dynamic flash combustion of the sample (at 1800°C) followed by reduction, trapping, complete GC separation and detection of the products. The instrument is a) fully automated and controlled by PC via the Eager 300 dedicated software, and b) capable of handling solid, liquid or gaseous substances.

2.1.2. Electron Spray Ionization Mass Spectrometry (ESI-MS) measurements. Electrospray ionization mass spectroscopy (ESI-MS) infusion experiments were carried out on a ThermoFisher Scientific model LTQ Orbitrap Discovery MS (Bremen, Germany). Compound **1**, containing quercetin as a ligand along with the aromatic chelator phen, was dissolved in methanol and introduced into the ESI source of the MS at a flow rate of 5 μL/min, using an integrated syringe pump. The infusion experiments were run using a standard ESI source operating in a negative ionization mode. Source operating conditions were a 3.7 kV spray voltage and a 300 ^{o}C heated capillary temperature.

2.1.3. Solution NMR Spectroscopy. Solution ^{1}H- and ^{13}C-NMR experiments for **1** were carried out on Varian 600 MHz spectrometer. The sample concentration was ~5 mM. Freshly prepared compounds were dissolved in deuterated dimethyl sulfoxide (DMSO-d_6). The spectra were run shortly after complete dissolution of the samples. Carbon spectra were acquired with 5000 transients, a spectral width of 37000 Hz and a relaxation delay of 2s. Proton spectra were acquired with 128 transients and a spectral width of 9000 Hz. Experimental data were processed using VNMR routines. Spectra were zero-filled and subjected to exponential apodization prior to FT. Chemical shifts (δ) are reported in ppm, while the spectrum was referenced by the standard experimental setup.

2.1.4. UV-Visible measurements. UV-Visible (UV-Vis) measurements were carried out on a Hitachi U2001 spectrophotometer in the range from 190 to 1000 nm.

2.1.5. Fluorescence measurements. Steady state fluorescence emission and excitation spectra were recorded on a Hitachi F-700 fluorescence spectrophotometer from Hitachi High-Technologies Corporation. The employed slit widths (em, ex) were 5.0 nm and the scan speed was 60 nm·min^{-1}. All measurements were carried out at room temperature. The entire system was supported by the appropriate computer software, FL Solutions 2.1, running on Windows XP.

2.1.6. Thermal studies. A Perkin Elmer, Pyris 1, system was used to run the simultaneous Thermogravimetric Analysis (TGA) experiments. The instrument mass precision is 1 μg.

About 10 mg of compound **1** was placed in an open alumina sample pan for each experiment. High purity air was used at a constant flow rate of 30 $mL \cdot min^{-1}$, depending on the conditions required for running the experiments. During the experiments, the sample weight loss and rate of weight loss were recorded continuously under dynamic conditions, as a function of time or temperature, in the range 30–850 °C. Prior to activating the heating routine program, the entire system was purged with the appropriate gas for 10 min, at a rate of 30 $mL \cdot min^{-1}$, to ensure that the desired environment had been established.

2.1.7. Electronic Structure Methodology. The Vienna Ab Initio Simulation Package (VASP), version 5.4.1. [**70**], was employed in order to study computationally the electronic structure of the cerium-quercetin complex. In terms of geometry optimization, the Perdew-Burke-Ernzerhof (PBE) gradient-corrected exchange-correlation functional [**71**] was used along with the Grimme DFT-D2 method [**72**], in which van der Waals interactions are described via a pair-wise force field. All calculations were performed using plane-wave basis sets and the projector augmented wave (PAW) method [**73,74**] with a plane-wave cut-off energy of 400 eV. In addition, a Γ centered k-point grid of 7×3×5 was employed for all calculations related to electronic structure, while geometry optimization involved a k-point grid of 1×1×1 with maximum residual atomic forces of 0.01 $eV \cdot Å^{-1}$. Gaussian smearing with a width of 0.05 eV was used to determine how partial occupancies are set for each wave function. The Ce(III)-QC-phen complex was optimized into a triclinic supercell (**Fig. S1**) of dimensions a = 11.14 Å, b = 19.08 Å, c = 16.82 Å, α = 89.9°, β = 91.8°, and γ = 90.0°, with a unit-cell volume of 3572.63 $Å^3$; initial crystal structure and atomic coordinates were taken from crystallographic data described in Section 2.3. Illustrations of the computational structures in this work were constructed using the visualization tool VESTA [**75**].

2.1.8. *In silico* computational methods

The *in silico* prediction tools employed in the study of the interaction of the compounds with the selected macromolecules, are Schrödinger, Mercury, Spartan' 14 and PyMol molecular modeling software. The synthesized complexes (with the exception of complexes 2 and 5) were generated from their X-ray crystal structures as CIF files. Mercury software (http://www.ccdc.cam.ac.uk/) was then used to convert the CIF files to PDB format files. Complexes 2 and 5 were built with the aid of ChemBioDraw Ultra v. 14.0.0.117 software and their structures were optimized with MM2 energy minimization force field method with the aid of ChemBio3D Ultra v. 14.0.0.117 software suite (CambridgeSoft Corporation).

The structures of quercetin (QC) and 1,10-phenanthroline (phen) were retrieved from NCBI (QC: CID_5280343, and phen: CID_1318). 3D conformers of structures were each built with the aid of ChemBio3D Ultra v. 14.0.0.117 and after structure optimization through energy minimization, pdb files of each structure were generated.

2.1.8.1. Molecular modelling

The molecular docking study was carried out on the crystal structure of *Saccharomyces cerevisiae* DNA, DNA gyrase, and glutathione S-transferase target macromolecules (Protein Data Bank, PDB entry codes 1YTF, 1KZN and 3IBH, respectively), in an attempt to investigate the effect of compound **1** on these target macromolecules. X-ray crystal structures of yeast transcription factor IIA (TFIIA) in complex with the TATA-box-binding protein (TBP) and TATA-element DNA (TFIIA/TBP/DNA complex) at 2.5 Å resolution (used only the DNA coordinates) [**76**], DNA gyrase in complex with bound co-crystallized drug chlorobiocin (CBN) [**77**], refined at 2.30 Å resolution, and yeast *S. cerevisiae* glutathione-S-transferase Gtt2 in complex with glutathione (GSH) [**78**] refined at 2.10 Å resolution, were obtained from the Brookhaven Protein Data Bank (operated by the Research Collaboratory for Structural Bioinformatics, RCSB) [**79**,**80**,**81**].

2.1.8.2. Docking calculations

In the present work, molecular docking calculations were performed with the Schrödinger modeling suite, having the ability for accurate calculations. The Schrödinger software suite contains a broad array of computational chemistry tools. In the procedure, for molecular docking through the Schrödinger suite, all compounds were drawn and converted into three-dimensional MOL2 files using Schrödinger Release 2017-1 Maestro Version 11.1 and minimized using LigPrep 3.4 [**82**] (which can generate a number of structures from each input structure, with various ionization states, tautomers, stereochemical characteristics, and ring conformations in order to eliminate molecules on the basis of various criteria, such as molecular mass or specified numbers and types of functional groups with correct chiralities for each successfully processed input structure), and the OPLS3 (**O**ptimized **P**otential for **L**iquid **S**imulations) [**83**] force field for optimization, thereby producing the low-energy isomers of the ligands (Schrödinger, http://www.schrodinger.com). Energy minimized 3D molecular structures were generated upon employment of LigPrep run from the Maestro utility of the Schrödinger suite. The ligand preparation included 2D–3D conversions, generating variations, correction, verification and optimization of the structures. Preparation of receptor and ligand structures was integrated before the actual docking procedure [**84**]. The crystal structures of proteins were prepared using the Protein Preparation Wizard [**85**], in

Schrödinger Suite 2015-2 (Schrödinger, LLC, New York, NY) [**86,87**]. A protein was prepared by adding the hydrogen atoms, optimizing hydrogen bonds, removing atomic clashes, adding formal charges to the hetero groups and then optimizing at neutral pH. Missing loops and side chains were prepared using Prime version 3.2 [**88,89**]. Finally, the structure was minimized using OPLS3 force field. Active sites of studied proteins were obtained using the SiteMap tool [**90,91**], which provides a fast and effective means of identifying potential binding pockets of proteins. SiteMap identifies the character of binding sites using a novel search and assesses each site by calculating various properties like size, volume, amino acid exposure, enclosure, contact, hydrophobicity, hydrophilicity and donor/acceptor ratio. Receptor grid was generated around the active site for effective binding using Receptor grid generation in the Glide (version 5.9) application of Maestro. Once the receptor grid has been generated, the ligands are docked to the proteins using the Glide docking tool of Schrödinger (**G**rid based **LI**gand **D**ocking with **E**nergetics) [**92**]. Compounds were docked in the binding site of the proteins using Induced-Fit Docking (IFD) protocol 2017-1 [**93,94,95**]. The ligand interactions are shown in the Ligand interaction tool of Maestro (Schrödinger). Waters were deleted with Maestro, the graphical user interface (GUI) of Schrödinger software, prior to docking. Molecular docking studies were carried out for the best fitted compounds to the model, with the final selection criteria being compound docking scores and the presence of crucial interactions for binding to the studied proteins [**96**]. The resulting poses were examined manually and the most promising ones were redocked with IFD calculations. Poses that pass the initial screens enter the final stage of the algorithm, which involves evaluation and minimization of a grid approximation to the OPLS-AA nonbonded ligand-receptor interaction energy. Final scoring is then carried out on the energy-minimized poses. By default, Schrödinger's proprietary GlideScore [**92**] multi-ligand scoring function is used to score the poses. Rescoring was performed to calculate and improved binding energy calculations with Prime's Molecular Mechanics-Generalized Born Surface Area (MM-GBSA) protocol, using the VSGB solvation model [**97,98**]. All complexes showed good docking scores, reflecting drug-binding affinities with the studied proteins. PyMol Molecular Graphics System (Schrödinger, LLC. version 1.8.2.0, www.pymol.org) [**99**] was used to visualize the molecules, analyze the docking results, and construct the molecular models.

2.2. Synthesis of [Ce($C_{15}H_9O_7$)($C_{12}H_8N_2$)(NO_3)$_3$]($C_{12}H_9N_2$)·CH_3OH (1)

An orange mixture of 0.22 g (0.50 mmoL) $Ce(NO_3)_3 \cdot 6H_2O$, 0.15 g (0.50 mmoL) quercetin dehydrate, and 0.10 g (0.55 mmoL) phen was placed in a round bottom flask, in the sequence

specified, and dissolved in 10 mL of methanol. The reaction mixture was stirred for ½ h. Then, it was placed in a teflon-lined stainless-steel reactor (23 mL) and heated to 80 ^{o}C for 2 h. Subsequently, the reactor was allowed to cool down to room temperature. The red crystals forming as a result of the process were isolated by filtration and dried in vacuo. The yield was 0.2 g (~37%). Anal. Calcd for **1**, **[Ce($C_{15}H_9O_7$)($C_{12}H_8N_2$)(NO_3)$_3$][$C_{12}H_9N_2$)·CH_3OH (1)**. ($C_{40}H_{30}N_7O_{17}Ce$ M_r 1020.83): C, 47.02; H, 2.94; N 9.60. Found: C, 47.04; H, 2.93; N 9.56. HR-ESI-MS (positive mode), calc. for $[Ce(C_{15}H_9O_7)(C_{12}H_8N_2)]^{2+}$, with m/z = 622.0107, z=1 (**Fig. 2**).

2.3. X-ray crystal structure determination. X-ray quality crystals of compound **1** were grown from a mixture of methanol-diethyl ether. Crystals were taken from the mother liquor and mounted at room temperature on a Bruker Kappa APEX 2 diffractometer, equipped with a triumph monochromator, using Mo Kα radiation. Cell dimensions and crystal system determination were performed using 211 high θ reflections with 15^{o}<θ<20^{o}). Data collection (φ- and ω- scans) and processing (cell refinement, data reduction and numerical absorption correction based on dimensions) were performed using the SAINT and SADABS programs [**100,101**]. The structure was solved by SUPERFLIP package [**102**]. The CRYSTALS version 14.61 build 6236 program package was used for structure refinement by full-matrix least-squares methods on F^2 and all subsequently remaining calculations [**103**]. Molecular illustrations were drawn with use of the Diamond 3.1 crystallographic package [**104**]. One phenolic group was found disordered over two positions with occupancy factors 0.6 for O(6) and 0.4 for O(8). Their hydrogen atoms were positioned geometrically to form hydrogen bonds. On the carbon atoms connected to these disordered phenolic groups, the missing hydrogen atom parts were positioned in order to obtain a proper formula for the compound. The oxygen atoms of the lattice methanol molecule were also found disordered over two equivalent positions. All non-hydrogen atoms were anisotropically refined. All non-disordered hydrogen atoms were found at their expected positions and refined using proper riding constraints to the pivot atoms. Crystallographic details for compound **1** are summarized in **Table 1**. Further details on the crystallographic studies as well as atomic displacement parameters are given as Supporting Information as well as in the form of cif files.

2.4. Biological studies

2.4.1. Effect of compound 1 and its components on baker's yeast growth. Lyophilized baker's yeast cells (*S. cerevisiae*) were suspended in a minimal medium salt (MMS),

containing 1.5% (w/v) glucose, 0.5% (w/v) NH_4Cl, 0.5% (w/v) K_2HPO_4, 0.1% (w/v) NaCl, 0.01% (w/v) $MgSO_4 \cdot 7H_2O$, and 0.1% (w/v) yeast extract, at a final concentration of 0.2 mg of cells/mL. Cells were grown overnight in an incubator, at 30 ^oC under 140 rpm constant shaking and the growth of the culture was monitored by measuring turbidity/absorbance at 600 nm on a Selecta UV-2005 UV-Vis spectrophotometer. To that end, cells were diluted with fresh MMS to obtain cultures of ~0.4 turbidity and were then allowed to grow for 24 h at 30 ^oC under 200 rpm constant shaking, following exposure to either compound **1** or its components [QC, phen, $Ce(NO_3)_3$] at several concentrations. Dimethyl sulfoxide (DMSO) 50% (v/v) was used to dissolve/dilute compound **1**, QC, and phen, whereas $Ce(NO_3)_3$ was dissolved/diluted in d.d. H_2O. The final DMSO concentration was adjusted in all cases to 1% v/v, which is not toxic to yeast cells. Turbidity of the cultures was measured and graphed, as a function of substance concentration, to evaluate their effect on cell growth and determine the IC_{50} value. Origin Pro 9.0 (OriginLab) was used for the construction of all graphs and GraphPad Prism 6 (GraphPad Software, Inc.) for the calculation of IC_{50} values. Cells from the respective cultures were harvested under centrifugation at 4,000 rpm for 10 min and then frozen, along with their extracellular media, for further analysis, at -20 ^oC.

2.4.2. Determination of yeast viability in cultures containing compound 1. Yeast viability, in the absence and presence of various concentrations of compound **1**, was assessed by determining the ability of enzymatic hydrolysis of fluorescein diacetate (FDA) to fluorescein by *S. cerevisiae* cultures. A stock solution of FDA in acetone (2 mg/mL) was added to reach a final FDA concentration of 10 μg/mL and the cultures were incubated at 30 ^oC on a rotary shaker (120 rpm) for 30 min. One volume of acetone was added to terminate the reaction and extract released fluorescein. Following centrifugation, the supernatants were recovered and then fluorescence was measured on an F-7000 FL Spectrophotometer (λ_{ex} = 494.0 nm; λ_{em} = 500-560 nm). The slit width was set at 2.5 nm.

2.4.3. Antibacterial effect of compound 1 and QC. The potential antibacterial effect of QC and compound **1** was tested with the well diffusion method. To that end, *Escherichia coli*, *Bacillus cereus* and *Staphylococcus aureus* were grown in LB broth overnight, at 37 ^oC under 140 rpm shaking, in an incubator. The cell cultures were then diluted with NaCl 0.9% (w/v) to reach a turbidity of 0.1. Several quantities from a stock solution (5 mg/mL) of QC or compound **1** in 50% DMSO, were injected into 1 cm diameter-cylindrical wells carved into LB agar plates and 100 μL of the diluted cultures were spread upon the agar surface. Inhibition of bacterial growth is reported in accordance with the diameter of the inhibition

zone around the wells. An amount of 100 μg of kanamycin (km) was used as a positive control and pure DMSO as a negative control.

2.4.4. Effect of Compound 1 on *S. cerevisiae* genomic DNA. Genomic DNA from yeast cells exposed to several concentrations of compound **1** was extracted as described previously [1]. Briefly, cells from 1.5 mL of culture were pelleted and stressed for lysis by repeated snap freezing-thawing cycles, followed by vortexing, in a buffer of 2% Triton X-100, 1% SDS, 100 mM NaCl, 10 mM Tris-HCl, 1 mM EDTA, pH 8.0. Then, 200 μL of chloroform was added, the mixture was centrifuged at 13,500 rpm for 10 min and the aqueous phase was collected. A volume of 400 μL of ice-cold ethanol was added in the mixture and stayed in the freezer for 5 min, in order to precipitate DNA. Following centrifugation, a DNA pellet was dissolved in a buffer containing 5% (v/v) glycerol, 0.04% (w/v) bromophenol blue and was subjected to electrophoresis in a 1% (w/w) agarose gel, containing 10 μL of 1% (w/v) ethidium bromide, at 150 V for 30 min. Tris-borate buffer (1.08% Tris base, 0.55% boric acid, 2 mM EDTA, pH 8.3) was employed as running buffer. DNA bands were visualized under UV light.

2.4.5. Determination of ROS radicals in yeast cultures containing compound 1 and its components. ROS generated intracellularly by *S. cerevisiae*, as a response to the exposure of cells to various concentrations of compound **1** and its components, were measured via the nitroblue tetrazolium (NBT) reduction, as described by Becerra et al. [2]. A suspension of 100 μL yeast cell cultures was precipitated, resuspended in PBS and mixed with 500 μL of 1 mg/mL NBT solution. The reactions were run at 30 ^{o}C under shaking for 30 min and terminated with 100 μL of 0.1 N HCl. The mixtures were centrifuged at 13,500 rpm for 5 min and the resulting pellets were dispersed in 400 μL DMSO to dissolve-extract the formazan product. Subsequently, 700 μL of PBS was added, the mixtures were centrifuged once again, and the absorbance of the samples was measured at 575 nm against a blank containing DMSO and PBS. The absorbance of samples containing only the studied compounds, in the absence of NBT reagent, was also recorded and subtracted.

2.4.6. Determination of MDA levels in yeast cultures containing compound 1 and its components. An aliquot of 500 μL of culture media was collected from each of the studied cultures, to which 500 μL of thiobarbituric acid (TBA) reagent [0.188 g of TBA in 50 mL of 0.25 N HCl, 10% (w/v) trichloroacetic acid (TCA)] had been added. The above mixture was incubated at 95 ^{o}C for 60 min. As a blank, 500 μL of supernatants was diluted with 500 μL of 0.25 N HCl in 10% (w/v) TCA. Samples were cooled to room temperature, centrifuged at 10,000 rpm for 5 min and the absorption of the supernatant was recorded at λ_{max} = 532 nm to

estimate the formation of the colored MDA-TBA complex against the TBA reagent as a blank. The absorbance of samples containing only the studied compounds, in the absence of the TBA reagent, was also recorded and subtracted.

2.4.7. DPPH· scavenging assessment. Dipicryl-phenyl hydrazine (DPPH·) is a stable radical form with an absorbance maximum of 517 nm. The ability of either compound **1** or QC to scavenge free radicals, was tested by mixing several concentrations of the studied compounds with 0.1 mM DPPH in methanol. After vortexing and a 5-minute incubation at room temperature, the absorbance at 517 nm was recorded. The absorbance of samples containing only the studied compounds, without DPPH·, was also recorded and subtracted. The radical scavenging ability was calculated after subtracting blank values and by employing the equation: $100 - \frac{A_{sample}}{A_{control}}\%$.

3. Results

3.1. Synthesis. The synthetic exploration of the ternary Ce(III)-QC-phen system followed a carefully designed approach. To that end, the **[Ce($C_{15}H_9O_7$)($C_{12}H_8N_2$)(NO_3)$_3$]($C_{12}H_9N_2$)·CH_3OH (1)** material was synthesized in a facile fashion from simple reagents in alcoholic solution. In a typical reaction, $Ce(NO_3)_3 \cdot 6H_2O$ reacted with QC and phen using methanol as a solvent. The overall stoichiometric reaction leading to **1** is shown schematically below:

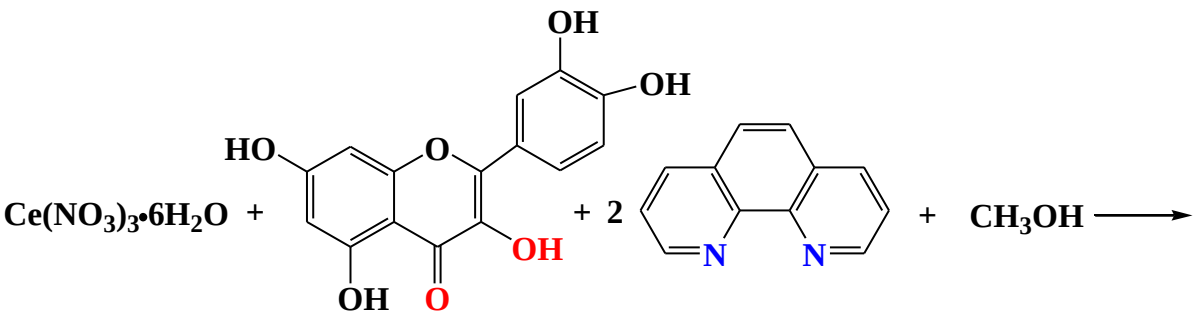

$[Ce(C_{15}H_9O_7)(C_{12}H_8N_2)(NO_3)_3]\bullet(C_{12}H_9N_2)\bullet(CH_3OH) + 6\ H_2O$

Diethyl ether was added as a precipitating solvent to the reaction mixture. Orange crystalline material emerged in the reaction described above, the analytical composition of which was consistent with the formulation in **1** (*vide supra*). Positive identification of the crystalline product was achieved by elemental analysis, FT-IR spectroscopy and X-ray crystallographic determination for isolated single crystals from **1** (*vide infra*). The complex is stable in the crystalline form, in the air, for fairly long periods of time. It is readily dissolved in methanol,

DMSO, and DMF, moderately soluble in water and ethanol, and insoluble in acetone, acetonitrile, and dichloromethane at room temperature.

3.2. Description of X-ray Crystallographic Structure

The X-ray crystal structure of **1** reveals a discrete solid-state lattice. The structure of the cerium assembly in **1** is shown in Figure **1A**. Selected bond distances and angles are listed in **Table 2**. Compound **1** crystallizes in the monoclinic space group $P2_1/n$. The asymmetric unit contains one monoanionic Ce(III) complex assembly, a singly protonated phen molecule and one lattice methanol molecule. The molecular structure of **1** shows a Ce(III) moiety bound to the chelating *N*,*N*-donor phen, singly deprotonated *O*,*O*-donor QC, and three nitrate anions, thus giving rise to a $Ce^{III}N_2O_8$ coordination sphere, in a rare, distorted mono-capped pentagonal square antiprismatic geometry. The antiprismatic geometry is formulated by two nearly parallel faces, one quadrilateral and one pentalateral. One additional coordinated atom forms a pyramid developed toward the site of the pentagonal face, thus completing the coordination polyhedron. Atoms O(1), O(2), O(13), and O(16) form the quadrilateral base, whereas O(9), O(10), O(12), O(15), and N(1) form the pentagonal base. The pentagonal pyramid forms as N(2) connects to the former pentagon (**Figure 1B**).

The Ce-N (phen) and Ce-O (QC) distances are in the range from 2.684(3) to 2.698(3) Å, and 2.324(3) to 2.685(3) Å, respectively. The Ce-N and Ce-O distances were found to be consistent with those reported in the literature [**105,106**].

Eleven hydrogen bonding interactions were found (**Table S1**), ultimately contributing to a two-dimensional (2D) crystal lattice. The lattice can best be described as one arising from planes of hydrogen-bonded complex anions parallel to the (a0c) crystallographic plane. The parallel planes formed are independent and between them lay co-parallel protonated phen cations interacting with the lattice methanol molecules being in close contact with the phenolic group containing O(8) (**Fig. 1C**).

3.3. FT-IR spectroscopy. The FT-IR spectrum of **1** indicates that complexation of Ce(III) ion by QC induces changes in the vibrational spectrum of the emerging complex assembly. In the FT-IR spectrum of free QC, the sharp absorption bands at 1666 cm^{-1} and 1610 cm^{-1} are assigned to the stretching vibration modes of C=O [**107**]. In the spectrum of **1**, absorption features between 1653 cm^{-1} and 1598 cm^{-1} indicate participation of this carbonyl moiety in the coordination sphere of the Ce(III) ion. The strong absorption band at 1455 cm^{-1} of QC, attributed to the δ(OH) vibrational mode [**108**], reduces its intensity and shifts to 1424 cm^{-1}, suggesting involvement of this group in the coordination sphere of the Ce(III) ion. The C-OH in plane deformation band appearing at 1261 cm^{-1} in the free QC shifts to 1297 cm^{-1} in

the complex assembly, usually observed when coordination involves the OH group [**109**]. The band at 815 cm^{-1} corresponds to the Ce-O stretching vibrations [**110,111**]. The bands of the phen moiety in the region from 1422 cm^{-1} to 1502 cm^{-1}, which are attributed to ring stretching vibrations, shift to higher frequencies upon chelation to the Ce(III) ion [**112**]. Similar shifts occur for the bands between 1294 cm^{-1} and 1090 cm^{-1}, while absorption bands in the region from 1040 cm^{-1} and 737 cm^{-1} shift to lower frequencies, with the splitting of the observed bands at 823 cm^{-1} and 726 cm^{-1} being indicative of out-of-plane C-H deformations [**113**]. All observations were further attested to by the X-ray crystal structure of **1**.

3.4. Solution NMR spectroscopy.

The room temperature ^{1}H-NMR and ^{13}C-NMR spectra of **1** in DMSO-d_6 (**Fig. 3A** and **3B**) showed characteristic spectral features of the Ce(III)-bound phen ligand and the quercetinato moiety. Chemical shifts are included in **Table 3**, enabling direct comparison between the solution-state shifts of free QC, phen, and **1**, with the estimated differences resulting from the equations:

$$\Delta\text{exp}' = \delta^{exp}_{compound\ \mathbf{1}} - \delta^{exp}_{free\ QC} \text{ and } \Delta\text{exp}' = \delta^{exp}_{compound\ \mathbf{1}} - \delta^{exp}_{free\ phen}$$

given in **Table 3** (in parentheses). Almost all carbon signals of coordinated QC exhibit downfield shifts as a result of coordination to the Ce(III) ion. Chemical shift changes due to complex formation are most pronounced for C(4), C(5), C(6), and C(10) of the coordinated QC ligand due to their close proximity to the Ce(III) ion in the complex assembly [**114**]. In the case of the coordinated phen, all carbons exhibit downfield coordination shifts characteristic of bound phen [**89**]. The ^{1}H-NMR spectrum of compound **1** demonstrates very sharp and distinct resonances for Ce(III)-bound quercetin. The deprotonation of the C(3)-OH group and the significant deshielding upon complexation of the C(3) and C(4) carbons clearly indicate that C(3)-OH and C(4)=O functional groups are the coordination sites [**115**]. As in the case of carbon signals, almost all hydrogen signals of the coordinated QC and phen ligands exhibit downfield shifts, compared to their unbound analogs, indicative of coordination to the Ce(III) ion [**116**].

3.5. UV-Visible spectroscopy. The UV–Vis spectra of pure QC and **1** were recorded in methanol at a concentration of 2.5x10^{-5} M (**Fig. 4**). Free QC as a flavone, exhibits two characteristic absorption bands [**117**]. The absorption band at 370 nm is related to the B-ring absorption of the cinnamoyl system (Band I) [**118**] and associated with n-σ^*, n-π^* and π-π^* transitions [**119**]. The strong absorption band at 254 nm corresponds to the A-ring absorption of the benzoyl system (Band II) [**85**] and corresponds to n-σ^*, and π-π^* transitions [**95-„122**].

In view of the aforementioned QC features, the electronic spectrum of **1** exhibits a similar pattern with the spectrum of QC, involving an intense absorption maximum of Band II at 260 nm (λ_{max}, ε ~68,640 $M^{-1}\cdot cm^{-1}$), indicating a bathochromic and hyperchromic shift to longer wavelength and higher absorbance. Band I, in the spectrum of **1**, also exhibits a bathochromic and hyperchromic shift (376 nm, ε ~35,400 $M^{-1}\cdot cm^{-1}$), compared to that of free QC. In general, literature reports suggest that the bathochromic shift in flavonoid complexes is caused either by a strong LMCT (Ligand to Metal Charge Transfer) process from the flavonoid to the metal ion center or a decrease in the HOMO-LUMO gap in the flavonoid molecule [84]. However, in the case of QC, theoretical calculations support a decrease of the HOMO-LUMO gap upon complexation of metal ions [**123,124**]. The extensive shift could be explained by considering the increased conjugation of the system caused by a new ring formation involving the C(3)-OH and C(4)=O groups and the coordination to the Ce(III) center [**125-128**]. Ligand centered bands, including among others the phen moiety, were present in the UV region (420 nm, ε ~22,680 $M^{-1}\cdot cm^{-1}$) [**129**].

3.6. Fluorescence studies. Steady state fluorescence measurements of emission and excitation spectra of pure QC and **1** were recorded in MeOH, at a concentration of $2.5x10^{-5}$ M and at room temperature (**Fig. 5**). The results at hand suggest that free QC exhibits an emission with two specific maxima at 431 nm and ~482 nm, when excited at 380 nm [**130,131**]. The emission spectrum of **1** shows a blue-shifted enhanced single broad band with an emission maximum at 488 nm, when excited at 430 nm. The observed signal enhancement is attributed to the intense complexation of QC to the Ce(III) ion, as also observed in other literature reports [**132**].

3.7. Thermal studies. The thermal decomposition of **1** was studied by TGA under an atmosphere of air (**Fig. 6A**). Compound **1** is thermally stable up to 275 °C. Between 275 ^{o}C and 403 ^{o}C, weight loss is observed, in line with the liberation of volatile substances and the decomposition of the organic structure of the parent molecule. No clear plateaus are reached in this temperature range, suggesting that the arising products are unstable and decompose further. A plateau in the decomposition of **1** is reached at 403 °C, with no further loss up to 850 °C, in line with the thesis that the product at that temperature and beyond (850 °C) is CeO_2. The total weight loss of ~83.0% is in good agreement with the theoretical value ~83.1%, according to the following equation:

$$2\{[Ce(C_{15}H_9O_7)(C_{12}H_8N_2)(NO_3)_3].(C_{12}H_9N_2)\cdot CH_3OH\} + 80O_2 \longrightarrow$$

$$2CeO_2 + 7N_2 + 80CO_2 + 30H_2O$$

Examination of the residue by powder XRD (**Fig. 6B**) showed the presence of CeO_2. These observations are consistent with previously reported results of TGA on cerium-containing species [**133**].

3.7. ESI-MS spectrometry. The ESI-MS spectru of Ce-quercetin-phen compound was investigated and recorded in methanol in a negative mode. The spectrum exhibited a pattern of three quadruplets, corresponding to Ce-containing molecular ions as following: M_1= $[M+NO_3+H]^-$, m/z=869.9671-872.9737 (z=1), M_2= $[M\text{-phen}]^-$, m/z=626.9037-629.9106 (z=1), M_3= $[M\text{-phen-}NO_3\text{-H}]^-$, m/z=563.9083-566.9156 (z=1) as shown in **Fig. 1**.

3.9. Electronic structure calculations. In order to look closely into the electronic structure of the Ce-quercetin complex, DFT calculations were performed following the procedure described in Section 2.1.9. The total density of states (DOS) as well as the projected density of states from individual contributions of Ce, C, N, and O atoms of the complex is shown in Fig. 7. The Fermi level (0 eV) is found to be located at ~0.4 eV above the conduction band minimum, which displays a major contribution from C, and O 2*p* orbitals and minimal hybridization from Ce 5*d* and N *2p* orbitals. To further investigate the origin of these states, the partial charge density diagram of the band above and below the Fermi level was plotted in Fig. 8, which are found to be strongly localized on the Ce atom and the surrounding C, O and N atoms. This provides evidence that the cerium ion acts as the coordination center, while carbon, oxygen and nitrogen atoms constitute part of the surrounding ligand, in agreement with experimental measurements described in Section 3.5. In order to quantify this picture, Bader charge analysis was performed to locate the amount of charge transfer occurring within the coordination assembly. It appears that, on average, for surrounding atoms (Fig. 1A), there is a charge reduction of ~0.9 |e| for N3, N4 and N5 atoms and ~1.2 |e| for C atoms closest to N1, N2, O1, and O2, while charge increase occurs by 1.1 |e| for Ce, ~1.6 |e| for O1 and O2, ~0.5 |e| for O9-O16, and 2.7 |e| for N1 and N2 atoms.

3.10. Biological in vitro Results

3.10.1. Toxicity of compound-1 and its components in yeast cells. For the evaluation of the effect of the newly synthesized compound **1**, baker's yeast cells were grown in the presence of various concentrations of the title compound. All free components participating in the assembly of **1**, namely $Ce(NO_3)_3$, QC, and phen, were also tested. The toxicity effect was

investigated by two methods: inhibition of cell growth by measuring turbidity (A_{600}) and inhibition of metabolic activity by determining the enzymatic capability of hydrolyzing the FDA ester.

As can seen in **Fig. 9**, the density of the employed cultures decreases significantly ($p<0.001$ for all concentrations tested above 2 μM) as the concentration of compound **1** increases, proving its high fungicidal capacity ($IC_{50} = 11 \pm 1$ μM). The toxicity of QC and $Ce(NO_3)_3$ in yeast cells is much lower and not statistically significant ($IC_{50} = 45 \pm 8.5$ μM, and $IC_{50} = 52 \pm 1.5$ μM, respectively). It is also interesting to note that in the presence of both QC and $Ce(NO_3)_3$, there seems to be a slight increase in yeast growth, reaching up to a significant ($p<0.01$) 13% level at 6 μM of QC and a 6% increase at 8 μM of $Ce(NO_3)_3$. Both compounds, however, are slightly toxic above 10 μM. 1,10-Phenanthroline toxicity is also significant ($p<0.001$ for all tested concentrations), but not as pronounced as that of compound **1** ($IC_{50} = 14 \pm 1.2$ μM).

To evaluate the inhibition of the metabolic activity by compound **1**, a viability assay was employed to test the capability of yeast cell enzymes to metabolize the fluorophore compound FDA. As depicted in **Fig. 10**, the viability of yeast cells decreases significantly as compound **1** concentration increases. These results are in agreement with those depicted in **Fig. 9**, thus verifying the fungicidal capacity of the newly synthesized material.

3.10.2. Effect of compound 1 on yeast genomic DNA. To evaluate the possible DNA damage occurring after exposure to the title compound, DNA was isolated from a) yeast cells exposed to several concentrations (2, 4, 6, 8, 10, and 20 μM) of **1**, and b) control cells (non-exposed). The resulting gel is given in **Fig. 11**. Two bands were visualized: one faint band above the level of the molecular markers (High) near the wells and another more intense band, at about the same level with the highest marker (10 kb) (Low). No DNA fragmentation was documented as an effect of cell exposure to the Ce complex. However, as the concentration of **1** increases, the intensity of the High band increases and at the same time the intensity of the Low band decreases (**Fig. 11**, lanes **3-7**). This observation may indicate possible aggregation of DNA under the influence of **1** or the DNA binding ability of **1** affording a high molecular mass complex of DNA with **1**, exemplified through an up-shift of a DNA part (portion) and manifested through reduced electrophoretic mobility of yeast DNA.

3.10.3. Effect of compound 1 and its components on the oxidative state of yeast cells. Two major markers of oxidative stress were studied: ROS and MDA – a product of lipid peroxidation. In **Fig. 12**, ROS levels of production/yeast cell density (%) are presented compared to control, as a result of the exposure to various concentrations of compound **1** or

its components (QC, Ce(III) and phen). Compound **1** imposes a significant increase on ROS levels in yeast cells, even at the lowest concentration tested. This increase parallels the significant decrease in yeast cell density and viability, proving that the cause of extreme oxidative stress, even at the lowest concentration (2 μM) tested, is the most likely mechanism of the fungicidal action of compound **1**. Surprisingly, however, all of the other compounds tested alone, lower the ROS levels significantly. More specifically, QC and Ce(III) almost completely diminish the ROS levels, thus attesting to their potent antioxidant capabilities.

On the other hand, MDA level of production/yeast cell density (%), as a result of cell exposure to various concentrations of compound **1** and its components, is shown at **Fig. 13**. Levels of MDA generation were higher than the control when yeast cells were incubated with all compounds. To that end, the observed behavior appears to be almost concentration-dependent and follows the order Ce(III)<QC<phen<compound **1**. The results may point out involvement of the lipid peroxidation mechanism in the toxicity of yeast cells. Moreover, they suggest a specific inhibition effect of all compounds on the $O_2^{\bullet -}$-radical scavenging mechanism of the fungal cells, thus increasing MDA levels, probably by inhibiting the enzymatic antioxidant potential.

3.10.4. Radical-scavenging abilities of compound 1 and QC. The scavenging capacity of both compound **1** and QC were assayed, employing the stable DPPH radical as a free radical model. The levels of DPPH radicals (%), under the influence of either compound **1** or QC, are shown in **Fig. 14**. The results suggest that both compounds are idle scavengers of free radicals up to the concentration of 40 μM. However, compound **1** is proven to be a more potent inhibitor (IC_{50} = 5.8 ± 1 μM) in comparison to pure QC (IC_{50} = 10.7 ± 1 μM).

3.10.5. Antibacterial ability of compound-1 and QC. The antibacterial capability of the newly synthesized compound **1** and of pure QC were tested with the "well-diffusion method". As seen in **Fig. 15a, b and c**, both compound **1** and QC possess antibacterial properties, as they inhibit dose-dependently the spread and growth of both Gram-negative (*E. coli*) and Gram-positive (*S. aureus*, *B. cereus*) bacteria. In all cases, the studied complex is significantly more efficient than pure QC, with the exception of 25 μg of either QC or compound **1** on Gram-positive bacteria, which project no differential effect. More specifically, in the case of *E. coli*, growth inhibition is pronounced even at the lowest studied amount of **1**, indicating possibly more pronounced sensitivity of Gram-negative bacteria to the studied compound. Km (100 μg) (**Fig. 11d**) was also employed as a model antibacterial compound along with pure DMSO. Km has indeed significantly inhibited growth of bacterial

colonies in all bacteria studied. Pure DMSO did not exhibit any effect on bacterial growth (image not shown).

3.10.6. In silico molecular docking calculations

Molecular docking calculations were employed to evaluate the ability of compound **1**, as well as its ligands QC and phen, to bind macromolecules, i.e. *Saccharomyces cerevisiae* DNA, DNA gyrase, and glutathione S-transferase, in order to explain the different *in vitro* activity of these compounds. Binding energies for the best docking poses of the compounds are shown in Table 4. From these data, it is obvious that compound **1** seems to achieve better binding (lower binding energy) for all targets, followed by compounds QC and phen. From the *in silico* prediction, the order of best binding activity is compound **1** > QC > phen. These data may in part explain the observed *in vitro* activities of the compounds themselves. The best scored pose of docked compound **1** with the lowest calculated free binding energy in each target macromolecule was selected for further visualization studies and evaluation of binding interactions.

3.10.7. Molecular docking calculations on *Saccharomyces cerevisiae* DNA. Our models for predicted binding poses of compound **1** and its ligands QC and phen into *S. Cerevisiae* DNA suggest intercalation of all molecules with A and B helices of DNA, between purines and pyrimidines of the same strand (intra-strand penetration) and between opposite strands as well (inter-strand penetration) in the minor groove, due to the emergence of van der Waals forces, hydrogen bond(s), and various types of π-π interactions or hydrophobic bonds (Fig. 16, Fig. 17). From Fig. 16, it is obvious that the docked compound **1** is buried deep in a binding cavity inside the minor groove of DNA, anchored through critical hydrogen bond (H-bond), π-π, π-polar, π-alkyl, and polar (P) interactions, with nucleotides of nine intra-strand base pairs: dC16≡dG1, dA15=dT2, dA14=dT3, dA13=dT4, dA12=dT5, dT11=dA6, dA10=dT7, dT9=dA8, and dA8=dT9 (between A and B strands of DNA) and intra-strand base pairs: dA15pdA14, dA14pdA13, dA13pdA12, dA12pdT11, dT11pdA10, dA10pdT9, and dT9pdA8 of DNA strand A (colored in deep teal), and dT2pdT3, dT3pdT4, dT4pdT5, dT5pdA6, dA6pdT7, and dT7pdA8 of DNA strand B (colored in deep purple), interrupting the inter-strand and also intra-strand hydrogen bond stabilization of the double-strand and single-strand of DNA (Fig. 16). The QC ligand of compound **1** is found to be inserted in the minor groove of DNA, in a perpendicular position to the parallel level of four base pairs, namely dT11=dA6, dA10=dT7, dT9=dA8, and dA8=dT9 (between A and B strands of DNA). Two of the nitrato ligands interrupt the dT11=dA6 and dA12=dT5 base pairs between

A and B strands of DNA, with the phen ligand being inserted in a perpendicular arrangement in the binding cavity and affecting the inter-strand H-bonding between another group of base pairs: dC16≡dG1, dA15=dT2, dA14=dT3, dA13=dT4 (between A and B strands of DNA).

It should be noted that compound **1** is inserted in the minor groove of DNA in such a way that its vertical axis (connecting the Ce center with QC and the phen moieties at the apical position) is parallel to the DNA helix axis (coinciding approximately with its vertical direction). This position of compound **1** results in the following angle definitions between nucleotide planes of either strands A and B and those of the two moieties of compound **1**: dA6(strand B)/QC (25.9^{o}), dT7/(strand B)/QC (35.9^{o}), dA8/(strand B)/QC (75.1^{o}), dA8/(strand A)/QC (71.3^{o}), dT9/(strand A)/QC (86.9^{o}), dA10/(strand A)/QC (48.1^{o}), dT11/(strand A)/QC (39.3^{o}), and dG1(strand B)/phen (33.8^{o}), dT2(strand B)/phen (26.6^{o}), dT3(strand B)/phen (73.5^{o}), dA15(strand A)/phen (60.5^{o}), dA14(strand A)/phen (24.9^{o}), and dA13(strand A)/phen (34.3^{o}).

The ligand-binding site architecture of the docked compound **1** in the crystal structure of DNA is illustrated in the lower panel of Fig. 16. Despite the bulk size of compound **1** and the fact that it is inserted in the more regionally restricted minor groove of the DNA, **1** adopts an orientation that allows it to enter the minor groove by its whole structure, as that is especially shown in the view above the axis of the DNA helix (upper right panel of Fig. 16), not in parallel to the base pair nucleobases, but rather in a perpendicular positioning covering nine base pair steps.

Intra-strand intercalation of complex **1** affects the single-stranded geometric stabilization of neighboring CpG or ApT base pair steps, thus influencing the overall helical model, whereas inter-strand intercalation induces an interruption of hydrogen bonds between G:C and A:P base pairs of the two clones, resulting in the destabilization of DNA duplex. Base stacking is the main stabilizing factor in the DNA duplex. Since **1** is placed between the DNA strands, interrupting the formation of hydrogen bonds between base pairs G:C and A:T, this orientation also affects base pair stacking. Thus, the interaction of **1** with CpG and ApT base pairs contributes to the destabilization in the overall helical model. Compound **1** is shown to interfere with numerous inter-strand base pairing dG≡dC and dA=dT interactions, invoking a perturbation in the canonical structure of the double helix, thereby influencing the functional role of the DNA. This is achieved by π-polar connection between the carbonyl O atom of the pyrimidine ring of guanine dG1 (B-strand) and the central ring of the phen ligand in **1**, distorting that way the inter-strand H-bond between the specific O and the cytosine dC16 (A-strand) amino hydrogen atom of the pyrimidine ring (3.5 Å). In the same way, the inter-

strand base pair dT2(B-strand)=dA15(A-strand) is interrupted, or at least distorted, by the formation of a π-polar contact between the thymine dT2 carbonyl O of the pyrimidine ring and the central ring of the phen ligand in **1** (2.6 Å). In the same base pairing, the amino group of dA15 is also π-polar connected to the central ring of the phen ligand in **1** (3.8 Å). The same holds true for the dT3(B-strand)=dA14(A-strand) base pair (2.8 Å for binding dT3 and 2.6 Å for binding dA14). The same type of interruption is observed for the dT4(B-strand)=dA13(A-strand) base pair. The amino group of dT4 pyrimidine ring of thymine is polar connected to both O (2.6 Å) and N (3.3 Å) atoms of the nitrato ligand coordinated to the central Ce atom. Furthermore, the amino group of the pyrimidine ring in adenine dA13, normally engaged into an H-bond with the carbonyl O of the pyrimidine ring in thymine dT4, is π-polar connected (2.5 Å) to the phen ring base pairing of **1**, perturbing the canonical inter-strand base pairing. Compound **1**, with the partition of the nitrato ligand O coordinated to Ce, also promotes an H-bond contact (3.1 Å) with the pyrimidine amino group of adenine dA12 (A-strand) (distortion of the H-bond base pairing with dT5 deoxynucleotide on the opposite B-strand). Nevertheless, dT5 is not interacting with any atom of **1**. Further destabilization of DNA pairing is achieved through π-polar contacts between the 3,4-dihydroxyphenyl ring (B) of the QC ligand in **1**, the carbonyl O of dT11 (2.4 Å), and the H-bond contact between the p-hydroxyl group O of the same ring in **1** and the amino hydrogen of dA6 of the opposite strand (2.5 Å), thus interrupting the dA6(B-strand)=dT11(A-strand) base pair. A similarly observed H-bond contact affects the dynamic nature of the dT7(B-strand)=dA10(A-strand) base pair with the carbonyl O of dT7, interacting with both hydroxyl groups of the 3,4-dihydroxyphenyl ring (B) of the QC ligand in **1** (2.7 Å, 3.7 Å), and the amino hydrogen of dA10 connected to both hydroxyl groups of the 3,4-dihydroxyphenyl ring (2.2 Å, 2.7 Å). Additional destabilization of the base pair is achieved through formation of the H-bond between the imine N atom of dA10 (taking part in the base pairing) and the p-OH group of the 3,4-dihydroxyphenyl ring (3.6 Å). A destabilization of the dA8(B-strand)=dT9(A-strand) base pair is also mediated by the inclusion of an H-bond between the meta hydroxyl O of the 3,4-dihydroxyphenyl ring and the amino hydrogen atom of dA8 (3.4 Å). Furthermore, the carbonyl O of dT9 is also H-bond connected to the meta hydrogen group of the same ring of the QC ligand (2.5 Å). Finally, the last base pair affected by compound **1** binding is dT9(B-strand)=dA8(A-strand), which is destabilized through formation of H-bonds between either the pentose O5 of dA8 or the OP2 of dT9 and the hydroxyl group of O4 atom of the chromene aromatic ring moiety in QC (2.1 Å and 3.0 Å, respectively). Additional destabilization is achieved by a π-polar contact of dT9/OP2 with

the aforementioned aromatic ring (2.5 Å). It appears, therefore, that the main action of compound **1** is to distort both inter-stranded base pairs and intra-strand neighboring base step structure of the DNA.

Compound **1** anchoring inside the minor groove of DNA is also facilitated by contacts of compound **1** with purines and pyrimidines of the same DNA strand, that way interrupting neighboring base step structure. These interactions involve the dT9pdA8 base pair of strand A: H-bond between a OH group of chromene moiety in QC with dA8/O5 (2.1 Å), dT9/OP2 (phosphate backbone) (3.0 Å), dA8/OP1(phosphate backbone) (2.3 Å), and π-polar contact with dT9/OP2 (2.5 Å) and dA8/OP2 (3.7 Å), π-polar contact between the 3,4-dihydroxypheyl moiety of QC and dA8/OP1 (2.8 Å), the dT7pdA8 base pair of strand B: H-bond between the OH groups of the 3,4-dihydroxypheyl moiety in QC with dA8/N6 (3.4 Å) and dT7/O4 (2.7 Å), dA10pdT9 base pair of strand A: H-bond between the OH groups of the 3,4-dihydroxypheyl moiety of QC with dA10/N6 (2.2 Å), and π-alkyl dT9/C7 (2.1 Å), and also the π-alkyl contact between the aromatic chromene aring moiety of QC with dT9/C7 (3.0 Å), dT9dT11pdA10 base pair of strand A: H-bond between the OH groups of the 3,4-dihydroxypheyl moiety of QC with dA10/N1 (3.6 Å), P contact with dT11/OP2 (3.0 Å) and π-alkyl contact of dT11/C7 (methyl of pyrimidine ring) with the former aromatic ring. Base stacking is the main stabilizing factor in the DNA duplex. Since compound **1** is placed between the DNA strands, inducing an interruption in the formation of H-bonds between both G:C and A:T base pairs, this orientation also affects base pair stacking. Further stabilization of compound **1** in the binding cavity of minor groove is mediated by π-π T-type interactions (edge-to-face) between the aromatic rings of the 3,4-dihydroxypheyl moiety of QC and dT11 (3.0-3.6 Å), dT9 (3.0-3.8 Å) of the A strand, the H-bond contact of dT9/O4 (strand B) with the 3'-OH group of the 3,4-dihydroxypheyl moiety (2.5 Å) contributing to a partial distortion of the dA8/N6 (amino H) (A strand) = dT9/O4 (carbonyl O) (B strand) base pair inter-strand H-bond connection, π-polar contacts between the aromatic ring of the 3,4-dihydroxypheyl moiety and dA6/N6 (B strand) (3.4 Å) and dT7/O4 (A strand) (3.9 Å). Additional perturbation of the DNA double helical structure is achieved by interrupting the hydrogen bond between the inter-strand base pairing through formation of various types of interactions, inducing a tension to numerous inter-strand base pairs. The stabilization of compound **1** is achieved through formation of a polar contact between the non-coordinated (to Ce) oxygen and nitrogen atoms of the bound nitrato ligand with dT4/O4 (B strand) (2.6 Å and 3.3 Å, respectively), interrupting the dA13=dT4 inter-strand base pair H-bonding, π-π T shape interactions between the phen aromatic ring of **1** and the imidazole rings of dG1 (B strand)

(2.5-2.8 Å) and dA13 (A strand) (2.9-3.7 Å), the pyrimidine ring of dT2 (B strand) (3.6-3.8 Å), π-polar interactions between the phen aromatic rings and dT2/O4 (B strand) (2.6 Å) (interrupting dT2=dA15 base pair), dT3/O4 (B strand) (3.7 Å), dG1/O5 (B strand) (2.9 Å) (interrupting dG1=dC16 base pair), dA14/N6 (A strand) (2.8 Å) (interrupting dT3=dA14 base pair), dG1/O6 (B strand) (3.5 Å), dA15/N6 (A strand)(4.0 Å), and dG1/N7 (B strand) (2.6 Å), and π-alkyl contacts between the phen aromatic rings and dT2/C7 (B strand) (3.7 Å).

Also shown in Fig. 17 are the docking orientations of compound **1** ligands QC and phen, docked individually, in the crystal structure of *S. cerevisiae* DNA, in the binding cavities of the minor groove of DNA. Both of these molecules seem to be able to enter the minor groove of DNA very deeply, as that is illustrated in a view above the axis of the helix on the right-hand side of Fig. 17.

3.10.8. Molecular docking calculations on DNA gyrase

Binding of compound **1** in the crystal structure of DNA gyrase is depicted in the upper part of Fig. 18, where the best-fitted docking pose of the molecule, exhibiting the lowest global binding energy, is depicted inside the ATP-binding site of DNA gyrase superimposed with the co-crystallized drug chlorobiocin (CBN). For the docking studies, we chose to use the crystal structure of DNA gyrase complexed with the co-crystallized aminocoumarin antibacterial inhibitor CBN, since several coumarine derivatives were reported to possess antifungal activity [**134,135,136,137,138,139**]. In the docking calculations, DNA gyrase involves only the B subunit, exhibiting the crucial ATPase activity (a subunit is mainly involved in DNA breakage and reunion) [**140,141**]. Compound **1** is shown to be stabilized inside the same binding pocket of the protein, occupied by CBN. Stabilization of compound **1** may be attributed to H-bond, hydrophobic (Hb), polar (P), π-polar, π-cation, π-anion, and π-alkyl contacts inside the ATP-binding site of DNA-gyrase protein. The ligand-binding site of **1** depicts the extent of the pocket as determined by the computation process, with labeling of the critical amino acid residues interacting with the molecule shown in the lower part of Fig. 18. The binding pocket is defined by a cavity of approximately 20 Å inside the B subunit of the protein that consists of two domains: an N-terminal domain of ~44 kDa and a C-terminal one of 47 kDa. The N-terminal domain includes two sub-domains (24 kDa C-terminal and 20 kDa N-terminal). The ATP-binding site is located in the first sub-domain of the protein, i.e., in the C-terminal part of the N-terminal domain. Docking predicts the emergence of a variety of interactions between compound **1** and the amino acid residues Asp45, Asn46, Asp49, Glu50, Asp73, Arg76, Gly77, Ile78, Pro79, Ala96, Gly119, Arg136, and THr165. CBN is stabilized in its binding pocket with the inclusion of the amino acid residues Asn46, Glu50,

Asp73, Ile90, Val120, and Arg136. Common binding residues of Cur and VCur with CBN appear to be Asn46, Glu50, Asp73, and Arg136. The rest of the binding residues of compound **1** are located adjacent to those of the CBN ligand. Compound **1** is shown to lie at the entrance of the catalytic pocket, partially covering the ATP-binding site. Stabilization of compound **1** in the enzyme binding cavity is achieved through formation of the following interactions: a number of H-bond contacts, demonstrated to facilitate binding of the molecule, such as between 3- and 4-hydroxyl groups of the 3,4-dihydroxypheyl moiety in QC and either Asp73/Oδ2 (2.2 Å, 2.8 Å) or Thr165/Oγ1 and N (2.6 Å and 2.7 Å), between the 7-hydroxyl group and O1 of the chromene aromatic ring moiety in QC and either Arg136/NH1 (2.5 Å) or Ile78/NH (3.7 Å), between all three equatorial nitrato ligands and Asp45/OH (2.9 Å), Asn46/Nδ2H (2.4 Å and 2.7 Å), and Asp49/Oδ1H (2.7 Å with the nitrato O and 3.0 Å with the nitrato N). Significant role in compound **1** anchoring also plays the formation of mixed π-type hydrophobic contacts (π-alkyl) between the aromatic ring of the 3,4-dihydroxypheyl moiety of QC and Thr165/Cβ (2.7 Å) and Glu50/Cγ (3.9 Å), between the chromene aromatic ring moiety of QC and Pro79/Cγ (3.7 Å), and between the phen aromatic ring and Gly119/Cα (3.3 Å). Other special interactions contributing to the stabilization of compound **1** involve π-charge electrostatic contacts, including π-cation between the negative charge of the chromene aromatic ring and the positive charge of the NH1 atom of the guanidinium group in Arg136 (2.9 Å) and Arg76 (3.9 Å), and a π-anion electrostatic contact between the aromatic ring of the 3,4-dihydroxypheyl moiety in QC and the negative charge of the Oδ1 carboxylic group (2.7 Å). Additional stabilization of the molecule is achieved through inclusion of π-polar interactions of the aromatic ring of the 3,4-dihydroxypheyl moiety of QC with Gly77/N (3.5 Å) and Thr165/Oγ1 (2.5 Å), the chromene aromatic ring moiety of QC with Gly77/O (3.2 Å) and Glu50/Oε2 (4.0 Å), between the phen aromatic ring and Ala96/O (2.3 Å) and Asn46/Nδ2 (2.4 Å), and a polar contact between the nitrogen atom of the nitrato ligand and Asn46/O (2.9 Å) and O1 of the chromene aromatic ring with Gly77/O (3.4 Å).

3.10.9. Molecular docking calculations on Glutathione S-transferase (GST)

A docking view orientation of compound **1** superimposed with QC, phen, and glutathione (GSH) is depicted in the upper part of Fig. 19. Our model for the predicted binding pose of **1** into the active site of GST, shows compound **1** lying inside the catalytic pocket of GST, between the glutathione (GSH)-binding site (G-site) and the electrophilic site (H-site), anchored in the protein through a number of binding contacts. The G-site is located at the N-terminus of the protein, whereas the H-site, located adjacent to the G-site, is found at the C-terminus. Compound **1** is found to be enclosed by α3, $\alpha4_a$, $\alpha4_b$, and α6 helices, whereas QC

and phen are surrounded by α1, α2, $\alpha4_b$ helices, and the loop connecting the β1 sheet with α1 helix and the β2 sheet with α2 helix. Compound **1** appears to be anchored in a binding pocket of the catalytic site, occupying only part of the primary binding H-site of the enzyme and more closely to the G-site. Actually, the 3,4-dihydroxypheyl moiety of QC in **1** is fully buried inside the H-site, with the chromene aromatic ring moiety of QC and the phen moiety slightly protruding from the cleft. Similarly, only the QC 3,4-dihydroxypheyl moiety and partly the phen ligand seem to be buried inside H-site. The docking orientation architecture of compound **1** and GSH in the active site of GST, illustrating the ligand binding interactions, is shown in the lower part of Fig. 19. Docking predicts the formation of a variety of interactions between compound **1** and the amino acid residues Tyr(Y)29 (α1 helix), Glu(E)85 (loop β4-α3), Cys(C)86 (α3 helix), Thr(T)87 (α3 helix), Lys(K)118 ($\alpha4_a$ helix), Glu(E)121 ($\alpha4_a$ helix), Leu(L)122 ($\alpha4_a$ helix), Asp(D)126 ($\alpha4_b$ helix), Ser(S)129 ($\alpha4_b$ helix), Val(V)130 ($\alpha4_b$ helix), and His(H)133 ($\alpha4_b$ helix). Glutathione (GSH) is stabilized in its binding pocket with the inclusion of the amino acid residues Tyr(Y)29, His(H)58 (α2 helix), Val(V)72 (loop β3-α2), Glu(E)85, Cys(C)86, Lys(K)118, Glu(E)121, and His(H)133 (underlined residues are common contacts with that of compound **1**). It is interesting that out of eight total binding contact residues, six are common with those of compound **1**. This is indicative that both molecules share the same binding cavity. On the contrary, QC and phen are positioned in an adjacent binding site.

Tight binding of compound **1** to the binding site of GST is mediated through a number of H-bond contacts, π-π stacking, π-polar, π-alkyl, and π-charge electrostatic interactions including π-anion, and π-cation. Significant role in anchoring of the molecule also plays the Tyr(Y)29 residue (of the α1 helix), mediating π-π stacking interactions through its aromatic ring with the aromatic ring of the 3,4-dihydroxypheyl moiety of the QC ligand in **1** (3.4-3.6 Å). The model for predicted binding modes of **1** into suggests that the complex assembly is stabilized in a cavity of the protein with a number of H-bond contacts between the 3-hydroxyl group of the 3,4-dihydroxypheyl moiety in QC with Ser(S)129/Oγ (2.7 Å) of the $\alpha4_b$ helix, between the N and O atoms of the nitrato ligand and Asp(D)126/Oδ1 (3.0 Å and 2.4 Å), and between the O atoms of the nitrato ligand and Glu(E)121/Oε2 (2.8 Å). Other special interactions contributing to the stabilization of **1** involve π-charge electrostatic contacts, including π-anion between the negative charge of the chromene aromatic ring and the negative charge of Asp126/Oδ2 (2.8 Å), and between the negative charge of the phen aromatic ring and Glu85/Oε1 (2.4 Å) (loop β4-α3), and π-cation between the negative charge of the phen aromatic ring and the positive charge of the terminal Nζ of Lys118 (2.7 Å). Significant role

in anchoring compound **1** also plays the formation of mixed π-type hydrophobic contacts (π-alkyl) between the aromatic ring of the 3,4-dihydroxypheyl moiety of QC and Val(V)130/Cγ2 (3.6 Å), the chromene aromatic ring and Leu(L)122/Cδ2 (4.0 Å), and the phen aromatic ring and Glu(E)85/Cβ (3.1 Å). Additional stabilization of the **1** is achieved through π-polar interactions of the aromatic ring of the 3,4-dihydroxypheyl moiety in QC with Asp(D)126/O (3.7 Å) and His(H)133/Cδ2 (4.1 Å) of the $\alpha 4_b$ helix, and between the phen ring and Cys(C)86/N (3.5 Å), Thr(T)87/Oγ1 and N (2.9 Å and 3.5 Å, respectively) (both residues at the edge of α3 helix). In addition, polar contacts are also observed between the O atoms of the nitrato ligand and Glu(E)121/Cβ (3.1 Å). Most interesting from the mechanistic point of view is the observation that there have been a number of binding contacts predicted between compound **1** and GSH. The revealed interactions form between all ligands of the complex assembly and the three amino acid residues of the tripeptide GSH (L-glutamyl-L-cysteinyl-glycine). Interactions include one H-bond between the 4-hydroxyl group of the 3,4-dihydroxypheyl moiety of QC and the peptide carbonyl O of the Gly-Cys moiety in GSH (2.7 Å), and two H-bonds between the nitrato ligand O atom with the carboxylic O atom of the Glu moiety in GSH (2.0 and 3.8 Å). Moreover, the GSH/compound **1** complex was stabilized through formation of π-polar contacts between the 3,4-dihydroxypheyl ring of **1** and the peptide carbonyl O of the Cys-Glu moiety in GSH (2.8 Å) and between the phen ring of **1** and the carboxylic O atom of the Glu moiety in GSH (3.1 Å). Docking also predicts the formation of a π-alkyl contact between the Glu moiety of GSH and the 3,4-dihydroxypheyl ring of compound **1**.

The intervention of compound **1** in the catalytic mechanism of GST, mediating conjugation of GSH to electrophilic centers *via* the sulfhydryl group, is accomplished through its H-bonding to His(H)133 that is known to act as the deprotonating moiety of the glutathione sulfur atom (stabilizing activity *via* H-bonding of GSH to His(H)133). It should be borne out that both molecules (compound **1** and GSH) bind to the same region of the active site.

Binding of compound **1** with GSH exemplifies the possibility of intervention in the GST activity, competing for the same catalytic binding site, close to the substrate GSH, using a comparable binding mode. Marginal binding of QC and phen with GSH was also documented, stabilized at the entrance of the shallow hydrophobic tunnel of the H-site. At the bottom of the H-site, the thiol group of GSH protrudes from the G-site over the amino-terminus of helix-α1.

The employed *in silico* prediction procedure implies that compound **1** can assume an inhibitory role against GST, consistent with the herein conducted *in vitro* antioxidant studies.

4. Discussion

4.1. Synthetic challenges in ternary lanthanide-QC systems

The bioactivity of natural polyphenolic compounds depends highly on their a) structural features, b) aqueous solubility and bioavailability, and c) biochemical reactivity with low and high molecular mass targets. Flavonoids are naturally derived substances (some of them glycosides), currently under investigation, of prime pharmaceutical significance due to their antioxidant properties and their beneficial role against cardiovascular and/or cancer pathologies. For a number of them, however, their poor aqueous solubility and bioavailability, controlled by the position of sugar groups and number of hydroxyl moieties, limit their specific and selective effectiveness toward development of efficient pharmaco-therapeutics. On the other hand, enhancement of such capacities through complexation to specific metal or lanthanide ions have been shown, through formulation of appropriate metal ion coordination environments, subsequently linked to exceptional beneficial activities toward the pathophysiology of cellular targets.

Cerium, as a member of rare earth elements, exerts diverse biological effects mainly due to the resemblance of the lighter lanthanides to calcium. This characteristic similarity enables calcium functional replacement by these elements in specific biomolecules [**142**]. Furthermore, the antiseptic, anti-inflammatory, and antineoplastic profile of cerium compounds has been well-documented [**110**]. In view of that lanthanide ion's (bio)chemical reactivity and QC's known bioactivity, the prospect of constructing binary and/or ternary cerium-QC complex assemblies (in the presence of ancillary ligands), with potential biological effectiveness, was pursued synthetically through the herein reported work. To that end, synthetic exploration of the ternary Ce(III)-QC-phen system in methanolic media led to the successful isolation of crystalline compound **1**. This is the only example of QC bound to a metal or lanthanide ion in a coordination environment confirmed through analytical, spectroscopic techniques and ultimately X-ray crystallography.

The use of the ancillary ligand in the stabilization of the ternary Ce(III)-QC-phen assembly (**1**) suggests that ternary systems of lanthanide ion-natural organic binder chelators, incorporating N,N-aromatic chelators in the complexation process, may lead to isolable crystalline products amenable to full spectroscopic, crystallographic, and biological characterization with enhanced hydrolytic stability for the bound QC.

4.2. The biology of the compound 1 and its free components

Flavonoids, like QC, have been studied extensively as promising, alternative supplements or medications to several chronic pathological conditions, such as neurodegeneration, cancer, and cardiovascular diseases [**143**]. Their antioxidant [**144,145**], anti-inflammatory [**146**] and antibacterial activities [**147**], are listed among some of their widely known beneficial properties. Owing to the aforementioned impediments in the solubility and bioavailability of such naturally occurring flavonoids, the herein achieved synthesis and isolation of the ternary Ce(III)-QC-phen compound **1** presents an opportunity to investigate a) changes occurring in the physicochemical profile of the flavonoid itself, as a results of its coordination to a metal ion and furthermore to a lanthanide ion such as Ce(III), and b) probe into and establish the biological profile of the flavonoid with respect to the known properties in physiology and pathological aberrations in humans, thereby attesting to either modulations (e.g. enhancement or diminution) of its activity toward antioxidant, anti-bacterial, anticarcinogenic, etc. properties or emergence of new properties as a result of its coordination to the metal center.

4.3. Growth inhibition

The newly synthesized compound **1** has been studied initially for its potential fungicidal and antibacterial activity. Yeast cells were grown in MMS medium for 24 h, at 30 ^{o}C, in the presence of various concentrations of compound **1**. Turbidity and viability measurements showed that **1** is an efficient fungicidal compound (IC_{50} = 11 ± 1 μM), far more toxic than pure QC or Ce(III) alone. 1,10-Phenanthroline, which was employed as a chelating agent, has also been shown to be significantly toxic against yeast cells, but less toxic than compound **1**. It is an established metal-chelator and is known to exhibit toxic effects on *S. cerevisiae* by binding zinc ions [**148**] and inducing genotoxicity [**149**].

4.4. Effect of Compound 1 on yeast genomic DNA.

For the evaluation of the possible cause of the observed toxicity of compound **1**, DNA damage and oxidative stress markers were studied. To that end, genomic DNA from cells exposed to compound **1** was isolated and electrophoresed through a 1% w/v agarose gel. No DNA damage (e.g. fragmentation) was noted on the gel, however a form of DNA aggregation or a more-dense packed DNA band was visualized, as the concentration of **1** increased, thus pointing toward the binding ability of compound **1** to DNA. Complexes containing phen were previously reported to bind yeast DNA and RNA [**150,151**]. Also, several flavonoids, including QC, are able to interact with eukaryotic DNA and induce topoisomerase-mediated DNA scission, yet concentrations tested were in the mM range [**152**]. Though not clear if the observed aggregation occurs pre- or post-lysis, DNA aggregation may explain inhibition of fungal growth, as that could lead to reduced DNA expression and duplication, and thus low

mitotic potential. More experiments are currently ongoing to study such effects of compound **1** on the yeast cell cycle.

4.5. Determination of ROS radicals and MDA in yeast cultures containing compound 1 and its components.

Flavonoids are able to reduce free radicals by either donating a hydrogen atom or a single electron, chelating radical-producing metal ions (Fe(II,III), Cu(I,II)), inhibiting ROS-producing enzymes, such as oxidases, lipoxygenases, and mitochondrial chain enzymes, or inducing antioxidant enzymes, such as UDP-glucuronosyltransferases, sulfotransferases, N-acetyltransferases, glutathione S-transferases, and methyltransferases [4].

In addition, the present work has demonstrated that exposure of yeast cells to **1** leads to increased oxidative stress, as proven by measuring both ROS and the hydroxy-radical marker MDA. Under the employed concentrations, **1** causes up to a 3-fold increase of ROS and up to a 4.5-fold increase in MDA levels, at 20 μM. Both of these results show that **1** significantly inhibits or diminishes the antioxidant mechanisms of fungal cells. Extreme oxidative stress is a main cause of toxicity, leading to extensive damage in the molecular content of the cell [**153**]. It is interesting that all of the free-unbound components of the newly synthesized complex reduce the ROS content of cells, with their reaction product being a strong agent of oxidative stress. It is intriguing that although phen is also toxic to yeast cells, it seems as if it acts as an ROS-scavenger, by lowering ROS levels by 50%. This effect cannot likely be attributed to phen itself, but rather to its metal ion-chelating ability. In fact, free iron ions are able to induce ROS production through the cell's oxidative metabolism [**154,155**]. MDA levels, however, are higher than control cells and this may also be a possible toxicity mechanism for phen. ROS produced in the cell could then oxidize lipids, with phen acting as a mediator in the electron transfer chain. QC and Ce(III) almost diminish ROS levels, as expected by two known radical-scavengers. Their antioxidant abilities may contribute to their positive effect on fungal growth up to 10 μM.

Indeed, it was previously described that incubation of *S. cerevisiae* with QC increases yeast defense against oxidative stress by reducing ROS levels and lowering glutathione oxidation, also increasing yeast cell lifespan. No effect of QC incubation on yeast superoxide dismutase (SOD) or catalase could be verified by the same study, though it was found to possess SOD-like activity in the tested cells [**156**]. In addition, Ce(III) ions have also been described as SOD-mimetic species [**157**]. SOD is a crucial enzyme for the antioxidant defense of all cells, turning free $O_2^{\bullet-}$ radicals into H_2O_2, subsequently transforming it through catalase to H_2O and O_2 [**158**]. Also, DPPH-scavenging experiments prove that both **1** and QC are good

scavengers of free radicals and the newly synthesized compound is a more efficient scavenger. It is, therefore, interesting to investigate the potential effect of **1** on the activity and expression of SOD and catalase and investigate whether their diminution or inhibition could explain the extreme oxidative stress noted in our results.

4.6. Antibacterial activity

Compound **1** and QC were studied in this work as potential antibacterial factors by employing a common test; that of the well-diffusion method. For these trials, common bacterial pathogens, namely *E. coli*, *S. aureus*, and *B. cereus* were employed and tested for their ability to grow and colonize the LB agar surface, under the influence of the tested compounds. Both **1** and QC inhibited growth and the spread of bacteria around the wells, but the effect induced by **1** was more pronounced, especially against the Gram-negative bacteria of *E. coli*. QC was previously found to possess antibacterial properties, by inducing aggregation of *S. aureus* cells and lower motility [**159,160**], inhibiting DNA gyrase in *E. coli* [**127,161**] and increasing permeability of the inner bacterial membrane [**127**]. More experiments, however, should be conducted in this case, in order to a) verify the antibacterial effect of **1** against these and other species of bacteria, and b) study the differential effect against either Gram-negative and Gram-positive bacteria.

The antibacterial effect of flavonoids is currently attributed to a plethora of reasons. Flavonoids can cause bacterial cell aggregation, accompanied by interference and chemical modification of the plasma membrane, reduced nucleic acid and cell wall synthesis and disruption of energy metabolism [**115**]. Disruption of bacterial biofilm is another mechanism for inhibition of bacterial growth [**162**]. As promising as it may seem, flavonoids' mostly non-polar nature is a crucial side-effect for their pharmaceutical applications, as they exhibit low bio-availability and bio-distribution [**111**]. To that end, employment of metal ions and chelating agents for synthesizing complex forms of flavonoids, is a rational approach to minimizing the massive, non-beneficial elimination of flavonoids [**163,164**]. In this work, such an approach has been invoked and adopted, thereby leading to the synthesis of a ternary Ce(III)-QC-phen complex and further investigation of its in vitro effect(s) on cellular experimental models, such as yeast cells and common pathogenic bacteria (*E. coli*, *S. aureus*, and *B. cereus*).

4.7. Molecular docking calculations

The ability of compound **1** to induce DNA aggregation can be attributed to its ability to a) disrupt DNA base pairing and simultaneously link two different DNA sites, and b) influence intra- and inter-strand base stacking, which is the main stabilizing factor in the DNA duplex.

Docking studies revealed that these perturbations of base stacking emerge as the main contributor to the destabilization of the DNA double helix. However, partial or full denaturation of DNA could not be ruled out. To achieve better understanding of the mechanism of action in place, a molecular dynamics (MD) simulation model should be adopted. The results show that both compound **1**, and QC and phen ligands can bind to the minor groove of DNA, as well as the active site of DNA gyrase and glutathione S-transferase, subsequently leading to inhibition of their activity.

The presented *in silico* study is in line with the *in vitro* inhibition experiments, supporting the DNA damage activity of compound **1** on yeast DNA, and also its fungicidal and antibacterial activity. Furthermore, an explanation of the increased oxidative stress of yeast cells following exposure to **1** by increasing ROS levels, caused by significant inhibition of the antioxidant mechanism of yeast cells, may be attributed, at least in part, to the inhibition of the antioxidant enzyme glutathione S-transferase (GST) by compound **1**.

A special interaction attracting compound **1** into the active site of GST is π-π stacking, which is prevalent in protein crystal structures, essentially contributing to the stabilization of a molecule in the binding site of the protein.

Significant role in compound **1** anchoring plays the formation of π-cation interactions, since cations bind to the π face of an aromatic structure through a surprisingly strong non-covalent binding. The interaction can be considered an electrostatic attraction between a positive charge of the small ligand molecule and the quadrupole moment of the aromatic system of the protein. Generally, interactions between an aromatic ring and a positive charge located above it have proven to be important in protein structure and biomolecule associations [**165,166,167,168**]. This phenomenon played a significant role in the inhibition of a) DNA gyrase, with the involvement of the positive charge of the guanidinium group of Arg136 and Arg76, and b) GST, with participation of the positive charge of the terminal nitrogen atom of the active site residue Lys118 (Nζ). Energetically, the π-cation interaction is comparable to or stronger than a hydrogen bond. Studies have suggested that the π-cation interaction is a a) powerful force aiding recognition between proteins and ligands, and b) valuable predictor of drug-receptor interactions. Similarly, π-anion interactions are also very important contributors to protein architecture and stability.

Since the phen and QC ligands dock away from the GSH molecule at the entrance of electrophilic site (H-site), it is not likely that they inhibit the GST enzyme significantly and thus they do not affect the antioxidant mechanism of fungal cells, a deduction in agreement with the finding that phen seems to act as an ROS scavenger by lowering ROS levels by 50%.

Similarly, QC and Ce(III) were found through *in vitro* experiments to almost diminish ROS levels, thus resulting in antioxidant activity and a positive effect on fungal cell growth (although compound **1** was found to possess more efficient scavenging activity compared to that of QC). Incubation of *S. cerevisiae* with QC seemed to increase yeast defense against oxidative stress by reducing ROS levels and lowering glutathione oxidation, thereby resulting in increased yeast cell populations. This is absolutely reasonable since flavonoids reduce free radicals by inhibiting ROS-producing enzymes, such as lipoxygenases, or inducing antioxidant enzymes such as GST. On the contrary, compound **1** was found to increase ROS levels in yeast cells, thereby inducing extreme oxidative stress. That way, compound **1** significantly inhibits the antioxidant mechanism of fungal cells, with a concomitant reduction on the cell population (fungicidal capacity of compound **1** with IC_{50} 11±1 μM, whereas QC and Ce(III) exhibit much lower fungicidal capacity with IC_{50} values 45±8.5 μM and 52±1.5 μM, respectively). That seems to be the most plausible mechanism for the fungicidal action of compound **1**. The latter contention can be explained, at least in part, by the *in silico* suggested inhibition of the antioxidant enzyme GST, since GST is an antioxidant and detoxification system that acts like a defense against oxidative attack via conjugation of electrophiles to glutathione (GSH) and reduction of lipid hyperoxides [**169**].

5. Conclusions

Efforts to modulate flavonoid chemical reactivity toward more soluble, bioavailable, and bioactive forms in cellular media led to the employment of the lanthanide cerium seeking interactions with the specific flavonoid in a ternary system containing a third ancillary ligand, namely the metal ion chelator phen. The synthetically pursued reactivity afforded a rare crystalline compound (**1**), the physicochemical analysis of which in the solid state and solution revealed structural characteristics of the coordination sphere of Ce(III) useful to its subsequent employment in biological investigations seeking out biochemical activity attributes. To that end, analytical, spectroscopic and crystallographic work portrayed a detailed picture of the ternary complex assembly comprised of Ce(III) chrysin and phen, with the undertaken theoretical work sustaining the picture of the solid-state coordination and lattice properties. Adjoining solution work complemented the solid-state properties and justified further *in vitro* biological work in various bacteria and yeast cultures. The results support a biochemically formulated picture that involves the flavonoid and the associated metal ion as well as chelator, pointing out individual contributions to the formulation of cell viability, oxidative stress and DNA interactive chemistry, thereby exemplifying salient

mechanistic pathways invoked to explain a wealth of phenotypic actions of the Ce(III) complex assembly. Concurrent *in silico* studies help gain deeper inside into interactions of **1** with key molecular targets in cells, thereby providing plausible explanatory information of the observations on its biological activity. The collective results project a well-defined profile of the ternary species of Ce(III), which in the presence of appropriate flavonoid(s) and organic chelators acquires biological activity attributes a) justifying its synthetic construction, and b) supporting efforts to further exploit flavonoids toward achievement of modulated protective roles in physiology and disease. The physicochemically supported biological phenotype for the well-defined complex assembly of chrysin and the lanthanide Ce(III) set the basis for further investigation of hybrid metal-organic assemblies as multifunctional materials in biological media, seeking out enhanced roles as metallodrugs or new bioactivity roles in the administration of (patho)physiological aberrations.

Acknowledgements

T.P. gratefully acknowledges use of Cirrus UK National Tier-2 HPC Service at EPCC, Edinburgh, under EPSRC grant EP/P020267/1.

Abbreviation list

AD	Alzheimer's disease
CBN	Chlorobiocin
DFT	Density Functional Theory
DPPH	Dipicryl-phenyl hydrazine
DMF	Dimethyl formamide
DMSO	Dimethyl sulfoxide
ESI-MS	Electrospray Spray Ionization Mass Spectrometry
FT-IR	FT-Infrared
GSH	Glutathione
GST	Glutathione S-transferase
GUI	Graphical user interface
HOMO	Highest Occupied Molecular Orbital
IFD	Induced-Fit Docking
Km	Kanamycin
LUMO	Lowest Unoccupied Molecular Orbital
MeOH	Methanol

MM-GBSA	Molecular Mechanics-Generalized Born Surface Area
NBT	Nitroblue tetrazolium
OPLS3	Optimized Potential for Liquid Simulations
PDB	Protein data bank
phen	1,10-Phenanthroline
QC	Quercetin
ROS	Reactive oxygen species
UV-Vis	UV-visible
NMR	Nuclear Magnetic Resonance
RCSB	Research Collaboratory for Structural Bioinformatics
TBA	Thiobarbituric acid
TBP	TATA-box-binding protein
TFIIA	Transcription factor IIA
TCA	Trichloroacetic acid
TGA	Thermogravimetric analysis

Appendix A. Supplementary data

Supplementary data on compound **1** in the form of figures were deposited as Supplementary Material (**Tables 1S-6S**, **Figs. S1-S2**). CCDC 2077242 (**1**) contains the supplementary crystallographic data for this paper. These data can be obtained free of charge via www.ccdc.cam.ac.uk/conts/retrieving.html (or from the Cambridge Crystallographic Data Centre, 12 Union Road, Cambridge CB21EZ, UK; fax: (+44) 1223-336-033; or deposit@ccde.cam.ac.uk).

References

1 M. M. Kasprzak, A. Erxleben, J. Ochocki, RSC Advances, 5 (2015) 45853-45877.

2 J. Cui, S. Li, Shaoshun, Mini-Rev. Med. Chem., 13 (2013) 1357-1368.

3 H. P. Kim, H. Park, Nat. Prod. Sci., 16 (2010) 59-67.

4 O. Burmistrova, M. T. Marrero, S. Estevez, I. Welsch, I. Brouard, J. Quintana, F. Estevez, Eur. J. Med. Chem., 84 (2014) 30-41.

5 S. Rubio, F. Leon, J. Quintana, S. Cutler and F. Estevez, Eur. J. Med. Chem., 55 (2012) 284-296.

6 E. Zyner, J. Graczyk, J. Ochocki, Pharmazie, 54 (1999) 945-946.

7 E. Corradini, P. Foglia, P. Giansanti, R. Gubbiotti, R. Samperi, A. Lagana, Nat. Prod. Res., 25 (2011) 469–495.

8 T. Guardia, A. E. Rotelli, A. O. Juarez, L. E. Pelzer, Il Farmaco, 56 (2001) 683–687.

9 G. Galati, P. J. O'Brien, Free Radic. Biol. Med., 37 (2004) 287- 303.

10 R. J. Williams, J. P. E. Spencer, C. Rice-Evans, Free Radic. Biol. Med., 36 (2004) 838-849.

11 M. Lopez-Lazaro, Mini-Rev. Med. Chem., 9 (2009) 31-59.

12 G. Rusak, I. Piantanida, L. Masic, K. Kapuralin, K. Durgo, N. Kopjar, Chem.-Biol. Interact., 188 (2010) 181-189.

13 A. H. Hegde, S. N. Prashanth, J. Seetharamappa, J. Pharm. Biomed. Anal., 63 (2012) 40-46.

14 I. B. Afanasev, A. I. Dorozhko, A. V. Brodskii, V. A. Kostyuk, A. I. Potapovitch, Biochem. Pharmacol., 38 (1989) 1763-1769.

15 L. Devi, M. Ohno, Neuropsychopharmacology, 37 (2012) 434-444.

16 J. P. Spencer, Chem. Soc. Rev., 38 (2009) 1152-1161.

17 W. Chen, S. Sun, W. Cao, Y. Liang, J. Song, J. Mol. Struct., 918 (2009) 194-197.

18 A. Priprem, J. Watanatorn, S. Sutthiparinyanont, W. Phachonpai, S. Muchimapura, Nanomedicine, 4 (2008) 70-78.

19 M. Fiorani, A. Guidarelli, M. Blasa, C. Azzolini, M. Candiracci, E. Piatti, O. Cantoni, J. Nutr. Biochem., 21 (2010) 397-404.

20 M. Kanter, C. Unsal, C. Aktas, M. Erboga, Toxicol. Ind. Health, 32 (2013) 541-550.

21 S. M. Choi, B. C. Kim, Y. H. Cho, K. H. Choi, J. Chang, M. S. Park, M. K. Kim, K. H. Cho, J. K. Kim, Chonnam Med. J., 50 (2014) 45-51.

22 C. M. Liu, G. H. Zheng, C. Cheng, J. M. Sun, J. Agric. Food Chem., 61 (2013) 7630-7635.

23 V. Garcia-Mediavilla, I. Crespo, P. S. Collado, A. Esteller, S. Sanchez-Campos, M. J. Tunon, J. Gonzalez-Gallego, Eur. J. Pharmacol., 557 (2007) 221-229.

24 S. Martinez-Florez, B. Gutierrez-Fernandez, S. Sanchez-Campos, J. Gonzalez- Gallego, M. J. Tunon, J. Nutr., 135 (2005) 1359-1365.

25 T. Banerjee, A. Van der Vliet, V. A. Ziboh, Prostagl. Leukot.Essent.Fat. Acids, 66 (2002) 485-492.

26 S. de Pascual-Teresa, K. L. Johnston, M. S. DuPont, K. A. O'Leary, P. W. Needs, L. M. Morgan, M. N. Clifford, Y. Bao, G. Williamson, J. Nutr., 134 (2004) 552-557.

27 C. H. Park, J. Y. Chang, E. R. Hahm, S. Park, H. K. Kim, C. H. Yang, Biochem. Biophys. Res. Commun., 328 (2005) 227-234.

28 G. L. Russo, M. Russo, C. Spagnuolo, I. Tedesco, S. Bilotto, R. Iannitti, R. Palumbo, Cancer Treat. Res., 159 (2014) 185-205.

29 M. Russo, C. Spagnuolo, I. Tedesco, S. Bilotto, G. L. Russo, Biochem. Pharmacol., 83 (2012) 6-15.

30 F. H. Psahoulia, S. Moumtzi, M. L. Roberts, T. Sasazuki, S. Shirasawa, A. Pintzas, Carcinogenesis, 28 (2007) 1021-1031.

31 M. Fiorani, A. Guidarelli, M. Blasa, C. Azzolini, M. Candiracci, E. Piatti, O. Cantoni, J. Nutr. Biochem., 21 (2010) 397-404.

32 K. A. Youdim, B. Shukitt-Hale, J. A. Joseph, Free Radic. Biol. Med., 37 (2004) 1683-1693.

33 R. Q. Yao, D. S. Qi, H. L. Yu, J. Liu, L. H. Yang, X. X. Wu, Neurochem. Res., 37 (2012) 2777-2786.

34 O. J. Lara-Guzman, J. H. Tabares-Guevara, Y. M. Leon-Varela, R. M. Alvarez, M. Roldan, J. A. Sierra, J. A. Londono-Londono, J. R. Ramirez-Pineda, J. Pharmacol. Exp. Ther., 343 (2012) 296-306.

35 R. J. Williams, J. P. Spencer, C. Rice-Evans, Free Radic. Biol. Med., 36 (2004) 838-849.

36 J. M. DimitricMarkovic, Z. S. Markovic, T. P. Brdaric, V. M. Pavelkic, M. B. Jadranin, Food Chemistry, 129 (2011) 1567-1577.

37 M. Balcerzak, A. Tyburska, E. Swiecicka-Fuchsel, Acta Pharm., 58 (2008) 327-334.

38 J. Ochocki, M. Kasprzak, L. Checinska, A. Erxleben, E. Zyner, L. Szmigiero, A. Garza-Ortiz, J. Reedijk, Dalton Trans., 39 (2010) 9711-9718.

39 M. Balcerzak, M. Kopacz, A. Kosiorek, E. Swiecicka, S. Kus, Anal. Sci., 20 (2004) 1333-1337.

40 M. Balcerzak, A. Kosiorek, E. Swiecicka, J. Anal. Chem., 61 (2006) 119-123.

41 A. Kosiorek-Rupinska, E. Swiecicka-Fuchsel, M. Balcerzak, Anal. Lett., 39 (2006) 589-602.

42 R. F. V. de Souza, E. M. Sussuchi, W. F. De Giovanni, Synth. React. Inorg. Met.-Org. Chem. 33 (2003) 1125-1144.

43 G. M. Escandar, L. F. Sala, Can. J. Chem., 69 (1991) 1994-2001.

44 M. T. Fernandez, L. Mira, M. H. Florencio, K. R. Jennings, J. Inorg. Biochem. 92 (2002) 105-111.

45 M. D. Engelmann, R. Hutcheson, I. F. Cheng, J. Agric. Food Chem., 53 (2005) 2953-2960.

46 A. Rygula, T. P. Wrobel, J. Szklarzewicz, M. Baranska, Vibr. Spectrosc., 64 (2013) 21-26.

47 G. Speier, V. Fulop, L. Parkanyi, J. Chem. Soc., Chem. Commun., 1990, 512-513.

48 E. Balogh-Hergovich, J. Kaizer, G. Speier, V. Fulop, L. Parkanyi, Inorg. Chem., 38 (1999) 3787-3795.

49 E. Balogh-Hergovich, G. Speier, G. Argay, J. Chem. Soc., Chem. Commun., 1991, 551-552.

50 E. Balogh-Hergovich, J. Kaizer, G. Speier, G. Argay, L. Parkanyi, J. Chem. Soc., Dalton Trans., 1999, 3847-3854.

51 F. B. A. El Amrani, L. Perello, J. A. Real, M. Gonzalez-Alvarez, G. Alzuet, J. Borras, S. Garcia-Granda, J. Montejo-Bernado, J. Inorg. Biochem., 100 (2006) 1208-1218.

52 E. Pieniazek, J. Kalembkiewicz, M. Dranka, E. Woznicka, J. Inorg. Biochem., 141 (2014) 180-187.

53 J. Kaizer, G. Barath, J. Pap, G. Speier, M. Giorgi, M. Reglier, Chem. Commun., (2007) 5235-5237.

54 Y. -J. Sun, Q. -Q. Huang, T. Tano, S. Itoh, Inorg. Chem., 52 (2013) 10936-10948.

55 G. Barath, J. Kaizer, G. Speier, L. Parkanyi, E. Kuzmann, A. Vertes, Chem. Commun., 2009, 3630-3632.

56 A. Matuz, M. Giorgi, G. Speier, J. Kaizer, Polyhedron, 63 (2013) 41-49.

57 K. Grubel, K. Rudzka, A. M. Arif, K. L. Klotz, J. A. Halfen, L. M. Berreau, Inorg. Chem., 49 (2010) 82-96.

58 E. Balogh-Hergovich, J. Kaizer, G. Speier, G. Huttner, A. Jacobi, Inorg. Chem., 39 (2000) 4224-4229.

59 E. Balogh-Hergovich, J. Kaizer, G. Speier, G. Huttner, L. Zsolnai, Inorg. Chim. Acta, 304 (2000) 72-77.

60 I. Lippai, G. Speier, G. Huttner, L. Zsolani, Acta Cryst., C53 (1997) 1547-1549.

61 J. Kaizer, J. Pap, G. Speier, L. Parkanyi, Eur. J. Inorg. Chem., (2004) 2253-2259.

62 I. Lippai and G. Speier, J. Mol. Catal. A, 130 (1998) 139-148.

63 I. Lippai, G. Speier, G. Huttner, L. Zsolnai, Chem. Commun., (1997) 741-742.

64 N. Okabe, E. Yamamoto, M. Yasunori, Acta Cryst., E59 (2003) m715-m716.

65 Y. -J. Sun, Q. -Q.Huang, J. -J. Zhang, Inorg. Chem., 53 (2014) 2932-2942.

66 W. Hiller, A. Nishinaga, A. Rieker, Z. Naturforsch., 47b (1992) 1185-1188.

67 E. Balogh-Hergovich, J. Kaizer, G. Speier, G. Huttner, P. Rutsch, Acta Cryst., C55 (1999) 557-558.

68 Y. Farina, B. M. Yamin, H.-K. Fun, B.-C.Yip, S.-G. Teoh, Acta Cryst., C51 (1995) 1537-1540.

69 M. M. Kasprzak, A. Erxleben, J. Ochocki, RSC Advances, 5 (2015) 45853-45877.

70 G. Kresse, J. Furthmüller, Phys. Rev. B, 54 (1996) 11169.

71 J. P. Perdew, K. Burke, M. Ernzerhof, Phys. Rev. Lett. 78 (1997) 1396.

72 S. Grimme, J. Comp. Chem. 27 (2006) 1787-1799.

73 P. E. Blöchl, Phys. Rev. B 50 (1994) 17953-17979.

74 G. Kresse, D. Joubert, Phys. Rev. B 59 (1999) 1758-1775.

75 K. Momma, F. Izumi, J. Appl. Crystallogr. 44 (2011) 1272-1276.

76 Tan S, Hunziker Y, Sargent DF, Richmond TJ. Crystal structure of a yeast TFIIA/TBP/DNA complex. Nature. 1996 May 9;381(6578):127-51. doi: 10.1038/381127a0.

77 D. Lafitte, V. Lamour, P. O. Tsvetkov, A. A. Makarov, M. Klich, P. Deprez, D. Moras, Claudette Briand, Robert Gilli. DNA Gyrase Interaction with Coumarin-Based Inhibitors: The Role of the Hydroxybenzoate Isopentenyl Moiety and the 5'-Methyl Group of the Noviose. Biochemistry (2002), 41, 7217-7223.

78 Ma XX, Jiang YL, He YX, Bao R, Chen Y, Zhou CZ. Structures of yeast glutathione-S-transferase Gtt2 reveal a new catalytic type of GST family. EMBO Rep. 2009 Dec;10(12):1320-6. doi: 10.1038/embor.2009.216.

79 H.M. Berman, J. Westbrook, Z. Feng, G. Gilliland, T.N. Bhat, H. Weissig, I.N. Shindyalov, P.E. Bourne, Nucleic Acids Res. 28 (2000) 235-242.
80 H.M. Berman, K. Henrick, H. Nakamura, Nature Struct. Mol. Biol. 10 (2003) 980.]
81 F.C. Bernstein, T.F. Koetzle, G.J. Williams, E.E. Meyer, M.D. Brice, J.E. Rodgers, O. Kennard, T. Shimanouchi, M. Tasumi, J. Mol. Biol. 112 (1977) 535-542.
82 K. Fosgerau, T. Hoffmann, Drug Discov. Today 20 (2015) 122-128.
83 D. Shivakumar, J. Williams, Y. Wu, W. Damm, J. Shelley, W. Sherman, J. Chem. Theory Comput. 6 (2010) 1509-1519.
84 G.M. Sastry, M. Adzhigirey, T. Day, R. Annabhimoju, W. Sherman, J. Comput. Aided Mol. Des. 27 (2013) 221-234.
85 G.M. Sastry, M. Adzhigirey, T. Day, R. Annabhimoju, W. Sherman, J. Comput-Aided Mol. Des. 27 (2013), 221-234.
86 R.A. Friesner, R.B. Murphy, M.P. Repasky, L.L Frye, J.R. Greenwood, T.A. Halgren, P.C. Sanschagrin, D.T. Mainz, J. Med. Chem. 49 (2006) 6177-6196.
87 T.A. Halgren, R.B. Murphy, R.A. Friesner, H.S. Beard, L.L. Frye, W.T. Pollard, J.L. Banks, J. Med. Chem. 47 (2004) 1750-1759.
88 M.P. Jacobson, D.L. Pincus, C.S. Rapp, T.J.F. Day, B. Honig, D.E. Shaw, R.A. Friesner, Proteins: Structure, Function and Bioinformatics 55 (2004) 351-367.
89 M.P. Jacobson, R.A. Friesner, Z. Xiang, B. Honig, J. Mol. Biol. 320 (2002) 597-608.]
90 T. Halgren, Chem. Biol. Drug Des. 69 (2007) 146-148.
91 T. Halgren, J. Chem. Inf. Model. 49 (2009) 377–389.
92 R.A. Friesner, J.L. Banks, R.B. Murphy, T.A. Halgren, J.J. Klicic, D.T. Mainz, M.P. Repasky, E.H. Knoll, D.E. Shaw, M. Shelley, J.K. Perry, P. Francis, P.S. Shenkin, J. Med. Chem. 47 (2004) 1739–1749.
93 R. Farid, T. Day, R.A. Friesner, R.A. Pearlstein, Bioorg. Med. Chem. 14 (2006) 3160-3173.
94 W. Sherman, T. Day, M.P. Jacobson, R.A. Friesner, R. Farid, J. Med. Chem. 49 (2006) 534-553.
95 W. Sherman, H.S. Beard, R. Farid, J. Med. Chem. 47 (2004) 1739–1749.
96 G.D. Geromichalos, C.E. Alifieris, E.G. Geromichalou, D.T. Trafalis, J. BUON 21 (2016) 764-779.
97 Bashford D, Case D.A. Generalized born models of macromolecular solvation effects. Annu Rev Phys Chem 2000; 51: 129–52
98 Li J, Abel R, Zhu K, *et al*. The VSGB 2.0 model: a next generation energy model for high resolution protein structure modeling. Proteins 2011; 79: 2794–812
99 W. L. DeLano The PyMol Molecular Graphics System 0.99, DeLano Scientific, San Carlos, CA, USA, 2006.
100 Bruker Analytical X-ray Systems, Inc. Apex2, Version 2 User Manual, M86-E01078, Madison, WI, (2006).
101 Siemens Industrial Automation, Inc. SADABS: Area-Detector Absorption Correction; Madison, WI, (1996).
102 P. W. Betteridge, J. R. Carruthers, R. I. Cooper, K. Prout, D. J. Watkin, J. Appl. Cryst., 36 (2003) 1487.
103 L. Palatinus, G. Chapuis, J. Appl. Cryst., 40 (2007) 786-790.

104 DIAMOND – Crystal and Molecular Structure Visualization, Ver. 3.1c, Crystal Impact, Bonn, Germany, (2006).

105 F. Ortu, H. Zhu, M. E. Boulon, David P. Mills, Inorganics, 3 (2015) 534-553.

106 B. D. Mahoney, N. A. Piro, P. J. Carroll, E. J. Schelter, Inorg. Chem., 52 (2013) 5970–5977.

107 V. A. Muñoz, G. V. Ferrari, M. I. Sancho, M. P. Montana, J. Chem. Eng. Data, 61 (2016) 987-995.

108 A. A.Ansari, Main Group Chem., 7 (2008) 133−145.

109 A.Pękal, M.Biesaga, K.Pyrzynska, BioMetals, 24 (2011) 41−49.

110 S. Thakur, P. Patil, Sensor Actuator B: Chemical, 194 (2014) 260-268.

111 A. Sharma, P. S. Kumar, Nanoscience Nanotechnology, 2 (2012) 82-85.

112 M. D. Grillone, F. Benetollo, G. Bombieri, Polyhedron, 10 (1991) 2171-2177.

113 A. K. Boudalis, V. Nastopoulos, S. P. Perlepes, C. P. Raptopoulou, A. Terzis, Transit. Metal Chem., 26 (2001) 276-281.

114 A. Ahmedova, K. Paradowska, I. Wawer, J. Inorg. Biochem. 110 (2012) 27-35.

115 A. Primikyri, G. Mazzone, C. Lekka, A. Tzakos, N. Russo, I. P. Gerothanassis, J. Phys. Chem. B, 119 (2015) 83-95.

116 M. Fréchette, I. R. Butler, R. Hynes, C. Detellier, Inorg. Chem., 31 (1992) 1650-1656.

117 J. Ren, S. Meng, C. E. Lekka, E. Kaxiras, J. Phys. Chem. B, 112 (2008) 1845-1850.

118 J. Joseph, K. Nagashri, Appl. Biochem. Biotechnol., 167 (2012) 1446-1458.

119 A. A. Ansari, Main Group Chem., 7 (2008) 15-30.

120 L. J. Porter, K. R. Markham, J. Chem. Soc., 0 (1970) 1309-1313.

121 M. E. Bodini, M. A. delValle, R. Tapia, F. Leighton, P. Berrios. Polyhedron, 20, (2001) 1005-1009.

122 E. B. Hergovich, J. Kaizer, G. Speier, G. Huttner, A. Jacobi. Inorg. Chem., 39 (2000) 4224-4229.

123 J. M. Dimitric Markovic, Z. S. Marlovic, T. P. Brdaric, N. D. Filipovic, Dalton Trans., 40 (2011) 4560-4571.

124 E. Balogh-Hergovich, J. Kaizer, G. Speier, G. Huttner, P. Rutsch, Acta Cryst., C55 (1999) 557-558.

125 N. Aliaga-Alcalde, P. Marqués-Gallego, M. Kraaijkamp, C. Herranz-Lancho, H. den Dulk, H. Gorner, O. Roubeau, S. J. Teat, T. Weyhermüller, J. Reedijk, Inorg. Chem. 49 (2010) 9655–9663.

126 M. Menelaou, T. Weyhermüller, M. Soler, N. Aliaga-Alcalde, Polyhedron 52 (2013) 398–405.

127 M. Menelaou, F. Ouharrou, L. Rodríguez, O. Roubeau, S. J. Teat, N. Aliaga-Alcalde, Chem.-Eur. J.18 (2012) 11545–11549.

128 N. Aliaga-Alcalde, L. Rodríguez, Inorg. Chim. Acta380 (2012) 187–193.

129 S. Banerjee, P. Prasad, A. Hussain, I. Khan, P. Kondaiah, A. R. Chakravarty, Chem. Commun. 48 (2012) 7702-7704.

130 I. Baran, C. Ganea, I. Ursu, V. Baran, O. Calinescu, A. Iftime, R. Ungureanu, I. T. Tofolean, Rom. Journ. Phys., 56 (2011) 388-398.

131 O. J. Rolinski, A. Martin,J. S. Birch, J. Biomed. Opt., 12 (2007) 034013

132 J. Zhou, L. Wang, J. Wang, N. Tang, J. Inorg. Biochem. 83 (2001) 41-48.

133 C. Duval, "Inorganic Thermogravimetric Analysis", Second and Revised Edition, Elsevier Publishing Co., Amsterdam, (1963).

134 C. Montagner, S. M. de Souza, C. Groposoa, F. Delle Monache, E. F A Smânia, A. Smânia Jr. Antifungal activity of coumarins. Z Naturforsch C J Biosci. 2008;63(1-2):21-8.

135 Q. Ji, Z. Ge, Z. Ge, K. Chen, H. Wu, X. Liu, Y. Huang, L. Yuan, X. Yang, F. Liao. Synthesis and biological evaluation of novel phosphoramidate derivatives of coumarin as chitin synthase inhibitors and antifungal agents. Eur J Med Chem. 2016 Jan 27;108:166-176.

136 R. Elias, R. Benhamou , Q. Z. Jaber, O. Dorot, S. L. Zada, K. Oved, E. Pichinuk, M. Fridman. Antifungal activity, mode of action variability, and subcellular distribution of coumarin-based antifungal azoles. Eur. J. Med. Chem. 179 (1) 2019, 779-790.

137 A. A. Al-Amiery, A. A. H. Kadhum, A. B. Mohamad. Antifungal Activities of New Coumarins. Molecules 2012, 17(5), 5713-5723.

138 S. Sardari, Y. Mori, K. Horita, R.G. Micetich, S. Nishibe, and M. Daneshtalab. Synthesis and antifungal activity of coumarins and angular furanocoumarins. Bioorg. Med. Cmem., 1999, 7, 1933-1940

139 S.U. Rehman, Z.H. Chohan, F. Gulnaz, and C.T. Supuran. In-vitro anribacterial, antifungal and cytotoxic activities of some coumarins and their metal complexes. J. Enzyme Inhib. Med. Chem. 2005, 204, 333-340.]

140 J.A. Ali, A.P. Jackson, A.J. Howells, A. Maxwell, Biochemistry 32 (1993) 2717-2724.

141 J.A. Ali, G. Orphanides, A. Maxwell, Biochemistry 34 (1995) 9801-9808.

142 M. A. Jakupec, P. Unfried, B.K. Keppler, Rev. Physiol. Biochem. Pharmacol., 153 (2005) 101-111.

[1] S. Harju, H. Fedosyuk, K.R. Peterson, Rapid isolation of yeast genomic DNA: Bust n' Grab, BMC Biotechnol. 4 (2004) 8. doi:10.1186/1472-6750-4-8.

[2] M.C. Becerra, A.J. Eraso, I. Albesa, Comparison of oxidative stress induced by ciprofloxacin and pyoverdin in bacteria and in leukocytes to evaluate toxicity, Luminescence. 18 (2003) 334–340. doi:10.1002/bio.742.

[143] A. Rodriguez-Mateos, D. Vauzour, C.G. Krueger, D. Shanmuganayagam, J. Reed, L. Calani, P. Mena, D. Del Rio, A. Crozier, Bioavailability, bioactivity and impact on health of dietary flavonoids and related compounds: an update., Arch. Toxicol. 88 (2014) 1803–53. doi:10.1007/s00204-014-1330-7.

[144] D. Procházková, I. Boušová, N. Wilhelmová, Antioxidant and prooxidant properties of flavonoids, Fitoterapia. 82 (2011) 513–523. doi:10.1016/j.fitote.2011.01.018.

[145] S.D.S. Banjarnahor, N. Artanti, Antioxidant properties of flavonoids, Med. J. Indones. (2015) 239. doi:10.13181/mji.v23i4.1015.

[146] G.H. Heeba, M.E. Mahmoud, A.A. El Hanafy, Anti-inflammatory potential of curcumin and quercetin in rats: role of oxidative stress, heme oxygenase-1 and TNF-α., Toxicol. Ind. Health. 30 (2014) 551–60. doi:10.1177/0748233712462444.

[147] T.P.T. Cushnie, A.J. Lamb, Recent advances in understanding the antibacterial properties of flavonoids., Int. J. Antimicrob. Agents. 38 (2011) 99–107. doi:10.1016/j.ijantimicag.2011.02.014.

[148] J.S. van Leeuwen, N.P.E. Vermeulen, J.C. Vos, Involvement of the pleiotropic drug resistance response, protein kinase C signaling, and altered zinc homeostasis in resistance of Saccharomyces cerevisiae to diclofenac., Appl. Environ. Microbiol. 77 (2011) 5973–80. doi:10.1128/AEM.00253-11.

[149] T. Bartos, S. Letzsch, M. Skarek, Z. Flegrová, P. Cupr, I. Holoubek, GFP assay as a sensitive eukaryotic screening model to detect toxic and genotoxic activity of azaarenes., Environ. Toxicol. 21 (2006) 343–8. doi:10.1002/tox.20190.

[150] K.L. Reddy, Y.H.K. Reddy, S. Satyanarayana, DNA-binding and photocleavage properties of Ru(II) polypyridyl complexes with DNA and their toxicity studies on eukaryotic microorganisms., Nucleosides. Nucleotides Nucleic Acids. 28 (2009) 953–68. doi:10.1080/15257770903307060.

[151] J. Liu, L.-F. Tan, L.-H. Jin, F. Luan, Synthesis, characterization, nucleic acid binding,

and cytotoxic activity of a Ru(II) polypyridyl complex., DNA Cell Biol. 31 (2012) 250–8. doi:10.1089/dna.2011.1307.

[152] F. Boege, T. Straub, A. Kehr, C. Boesenberg, K. Christiansen, A. Andersen, F. Jakob, J. Köhrle, Selected Novel Flavones Inhibit the DNA Binding or the DNA Religation Step of Eukaryotic Topoisomerase I, J. Biol. Chem. 271 (1996) 2262–2270. doi:10.1074/jbc.271.4.2262.

[153] S. V. Avery, Molecular targets of oxidative stress, Biochem. J. 434 (2011) 201–210. doi:10.1042/BJ20101695.

[154] R.E. Shackelford, R.P. Manuszak, C.D. Johnson, D.J. Hellrung, C.J. Link, S. Wang, Iron chelators increase the resistance of Ataxia telangeictasia cells to oxidative stress, DNA Repair (Amst). 3 (2004) 1263–1272. doi:10.1016/j.dnarep.2004.01.015.

[155] R. Sugimoto, Y. Kumagai, Y. Nakai, T. Ishii, 9,10-Phenanthraquinone in diesel exhaust particles downregulates Cu,Zn–SOD and HO-1 in human pulmonary epithelial cells: Intracellular iron scavenger 1,10-phenanthroline affords protection against apoptosis, Free Radic. Biol. Med. 38 (2005) 388–395. doi:10.1016/j.freeradbiomed.2004.11.003.

[156] I. Belinha, M.A. Amorim, P. Rodrigues, V. de Freitas, P. Moradas-Ferreira, N. Mateus, V. Costa, Quercetin Increases Oxidative Stress Resistance and Longevity in Saccharomyces cerevisiae, J. Agric. Food Chem. 55 (2007) 2446–2451. doi:10.1021/jf063302e.

[157] E.G. Heckert, A.S. Karakoti, S. Seal, W.T. Self, The role of cerium redox state in the SOD mimetic activity of nanoceria, Biomaterials. 29 (2008) 2705–2709. doi:10.1016/j.biomaterials.2008.03.014.

[158] E. Herrero, J. Ros, G. Bellí, E. Cabiscol, Redox control and oxidative stress in yeast cells, Biochim. Biophys. Acta - Gen. Subj. 1780 (2008) 1217–1235. doi:10.1016/j.bbagen.2007.12.004.

[159] O.K. Mirzoeva, R.N. Grishanin, P.C. Calder, Antimicrobial action of propolis and some of its components: the effects on growth, membrane potential and motility of bacteria., Microbiol. Res. 152 (1997) 239–46. doi:10.1016/S0944-5013(97)80034-1.

[160] I. Hirai, M. Okuno, R. Katsuma, N. Arita, M. Tachibana, Y. Yamamoto, Characterisation of anti-Staphylococcus aureus activity of quercetin, Int. J. Food Sci.

Technol. 45 (2010) 1250–1254. doi:10.1111/j.1365-2621.2010.02267.x.

[161] A. Plaper, M. Golob, I. Hafner, M. Oblak, T. Solmajer, R. Jerala, Characterization of quercetin binding site on DNA gyrase., Biochem. Biophys. Res. Commun. 306 (2003) 530–6. http://www.ncbi.nlm.nih.gov/pubmed/12804597.

[162] L.A.A. Lopes, J.B. Dos Santos Rodrigues, M. Magnani, E.L. de Souza, J.P. de Siqueira-Júnior, Inhibitory effects of flavonoids on biofilm formation by Staphylococcus aureus that overexpresses efflux protein genes., Microb. Pathog. 107 (2017) 193–197. doi:10.1016/j.micpath.2017.03.033.

[163] J. Jiang, S. Yao, H.-H. Cai, P.-H. Yang, J. Cai, Synthesis and synergetic effects of chrysin-organogermanium(IV) complex as potential anti-oxidant., Bioorg. Med. Chem. Lett. 23 (2013) 5727–32. doi:10.1016/j.bmcl.2013.07.073.

[164] Q.K. Panhwar, S. Memon, Synthesis of Cr(III)-morin complex: characterization and antioxidant study., ScientificWorldJournal. 2014 (2014) 845208. doi:10.1155/2014/845208.

165 Wintjens R, Liévin J, Rooman M, Buisine E. Contribution of cation-pi interactions to the stability of protein-DNA complexes. J Mol Biol. 2000 Sep 15;302(2):395-410. doi: 10.1006/jmbi.2000.4040. PMID: 10970741.

166 Gallivan JP, Dougherty DA. Cation-pi interactions in structural biology. Proc Natl Acad Sci U S A. 1999;96(17):9459-9464. doi:10.1073/pnas.96.17.9459

167 Dougherty DA. Cation-pi interactions in chemistry and biology: a new view of benzene, Phe, Tyr, and Trp. Science. 1996 Jan 12;271(5246):163-8. doi: 10.1126/science.271.5246.163.

168 Scrutton, N. S., & Raine, A. R. (1996). Cation-pi bonding and amino-aromatic interactions in the biomolecular recognition of substituted ammonium ligands. The Biochemical journal, 319 (Pt 1)(Pt 1), 1–8. doi: 10.1042/bj3190001

169 Röth E, Marczin N, Balatonyi B, et al. Effect of a glutathione S-transferase inhibitor on oxidative stress and ischemia-reperfusion-induced apoptotic signalling of cultured cardiomyocytes. Exp Clin Cardiol. 2011;16(3):92-96.

Table 1: Summary of Crystal, Intensity Collection and Refinement Data for $[Ce(C_{15}H_8O_7)(C_{12}H_8N_2)(NO_3)_3](C_{12}H_9N_2)\cdot CH_3OH$ **(1).**

Compound	**1**
Chemical formula	$C_{40}H_{30}CeN_7O_{17}$
Molecular mass	1020.83
Crystal system	monoclinic
Space group	$P2_1/n$
Temperature, ^oK	295
a (Å)	11.333(3)
b (Å)	20.249(5)
c (Å)	17.214(5)
α, deg	90°
β, deg	92.200(7)°
γ, deg	90°
V, (Å^3)	3947.3(18)
Z	4
Radiation type	MoK_a
Abs. coeff. (μ), mm^{-1}	1.24
Crystal size, (mm)	0.13 x 0.11 x 0.08
Data collection diffractometer	Bruker Kappa Apex2
Absorption correction	Numerical
T_{min}, T_{max}	0.87, 0.91
Wavelength, λ (Å)	0.71073
D_{calcd} (Mg m^{-3})	1.716
Measured, independent and observed reflections ($I>2.0\sigma(I)$)	39003,7543,6059
R_{int}	0.044
$R[F^2> 2\sigma(F^2)]$	0.0462
$R_w(F^2)$	0.0634
S	1.00
No. of reflections	6059
No. of parameters	604
No. of restraints	8
H-atom treatment	H atoms treated by a mixture of independent and constrained refinement
$\Delta\rho_{max}$, $\Delta\rho_{min}$ (e Å^{-3})	1.01, -1.01

Weighting Chebychev polynomial with $w = w' \times [1 - (\Delta F_{obs} / 6 \times \Delta F_{est})^2]^2$ and $w' = [P_0T_0'(x) + P_1T_1'(x) + ...+ P_{n-1}T_{n-1}'(x)]^{-1}$, where P_i are the coefficients of a Chebychev series in $t_i(x)$, and $x = F_{calc}^2/F_{calc}^2{}_{max}$. P_0 - P_{n-1} = 1.41 1.65 0.536

Table 2: Bond lengths [Å] and angles [deg] for $[Ce(C_{15}H_9O_7)(C_{12}H_8N_2)(NO_3)_3](C_{12}H_9N_2)\cdot CH_3OH$ **(1)**.

Bonds	**Bond length (Å)**	**Bonds**	**Bond length (Å)**
Ce(1)-O(1)	2.324(3)	Ce(1)-O(13)	2.649(3)
Ce(1)-O(2)	2.521(3)	Ce(1)-O(15)	2.651(3)
Ce(1)-O(9)	2.595(3)	Ce(1)-O(16)	2.610(3)
Ce(1)-O(10)	2.685(3)	Ce(1)-N(1)	2.689(3)
Ce(1)-O(12)	2.587(3)	Ce(1)-N(2)	2.698(3)
Angles	**(°)**	**Angles**	**(°)**
O(1)-Ce(1)-O(2)	65.39(9)	O(2)-Ce(1)-N(1)	78.09(10)
O(1)-Ce(1)-O(9)	76.80(12)	O(9)-Ce(1)-N(1)	77.04(11)
O(2)-Ce(1)-O(9)	76.78(11)	O(10)-Ce(1)-N(1)	113.63(11)
O(1)-Ce(1)-O(10)	67.71(10)	O(12)-Ce(1)-N(1)	128.08(11)
O(2)-Ce(1)-O(10)	112.82(10)	O(1)-Ce(1)-N(2)	137.87(10)
O(9)-Ce(1)-O(10)	47.46(10)	O(2)-Ce(1)-N(2)	133.91(10)
O(1)-Ce(1)-O(12)	92.34(10)	O(9)-Ce(1)-N(2)	74.37(11)
O(2)-Ce(1)-O(12)	150.66(10)	O(10)-Ce(1)-N(2)	70.17(10)
O(9)-Ce(1)-O(12)	118.25(11)	O(12)-Ce(1)-N(2)	75.41(10)
O(10)-Ce(1)-O(12)	71.92(11)	O(13)-Ce(1)-O(15)	66.85(11)
O(1)-Ce(1)-O(13)	74.07(11)	O(13)-Ce(1)-O(16)	67.11(10)
O(2)-Ce(1)-O(13)	105.21(11)	O(15)-Ce(1)-O(16)	47.98(9)
O(9)-Ce(1)-O(13)	146.45(11)	O(13)-Ce(1)-N(1)	136.48(11)
O(10)-Ce(1)-O(13)	104.97(11)	O(15)-Ce(1)-N(1)	72.18(11)
O(12)-Ce(1)-O(13)	47.78(11)	O(16)-Ce(1)-N(1)	74.98(11)
O(1)-Ce(1)-O(15)	139.15(11)	O(13)-Ce(1)-N(2)	118.68(11)
O(2)-Ce(1)-O(15)	113.62(9)	O(15)-Ce(1)-N(2)	74.69(10)
O(9)-Ce(1)-O(15)	144.04(11)	O(16)-Ce(1)-N(2)	116.13(10)
O(10)-Ce(1)-O(15)	133.32(9)	N(1)-Ce(1)-N(2)	60.95(10)
O(12)-Ce(1)-O(15)	70.20(10)		
O(1)-Ce(1)-O(16)	105.86(10)		
O(2)-Ce(1)-O(16)	67.66(10)		
O(9)-Ce(1)-O(16)	138.30(10)		
O(10)-Ce(1)-O(16)	171.39(10)		
O(12)-Ce(1)-O(16)	103.33(11)		
O(1)-Ce(1)-N(1)	138.89(10)		

Table 3: ^{1}H and ^{13}C chemical shifts for free QC, phen, and **1**.

Proton	**Free QC [91]**	**Compound 1**	**Carbon**	**Free QC [91]**	**Compound 1**
OH5	12.51	12.48 (0.03)	C(2)	147.20	146.62 (0.58)
OH7	10.85	10.78 (0.07)	C(3)	136.00	135.56 (0.44)
OH4′	9.65	9.59 (0.06)	C(4)	176.50	175.66 (0.84)
OH3	9.42	-	C(5)	161.40	160.54 (0.86)
OH3′	9.36	9.31 (0.05)	C(6)	98.80	98.00 (0.80)
H2′	7.68	7.67 (0.01)	C(7)	164.20	163.70 (0.50)
H6′	7.55	7.53 (0.02)	C(8)	93.90	93.17 (0.73)
H5′	6.88	6.88 (0.00)	C(9)	156.40	155.94 (0.46)
H8	6.41	6.39 (0.02)	C(10)	103.70	102.84 (0.86)
H6	6.19	6.17 (0.02)	C(1)′	122.30	121.78 (0.52)
			C(2)′	115.30	114.90 (0.40)
			C(3)′	145.50	145.37 (0.13)
			C(4)′	148.00	147.54 (0.46)
			C(5)′	115.40	115.43 (-0.03)
			C(6)′	120.20	119.80 (0.40)
	Free phen [92]			**Free phen [92]**	
C(11),C(11)′	9.17	9.08 (0.09)	C(11),C(11)′	151.24	149.77
C(12),C(12)′	7.77	7.76 (0.01)	C(12),C(12)′	124.43	123.13
C(13),C(13)′	8.45	8.47 (-0.02)	C(13),C(13)′	137.24	136.02
C(15),C(15)′	7.98	7.96 (0.02)	C(14),C(14)′	147.42	144.89
			C(15),C(15)′	127.96	126.51
			C(16),C(16)′	130.12	128.28

Table 4: Global binding energies (in kcal/mol) of compound **1**, QC, and phen docked on s. cerevisiae DNA, DNA gyrase and Glutathione S-transferase targets (PDB accession numbers: 1YTF, 1KZN and 3IBH respectively).

Compound	Bio-macromolecule		
	DNA	**DNA gyrase**	**Glutathione S-transferase**
1	**-55.82***	**-41.47***	**-27.71***
QC	-45.54	-37.91	*-13.39***
phen	*-35.15***	*-34.11***	-24.61

* denotes lowest binding energy (in bold phase)

** denotes highest binding energy (in italics)

Figure Captions

Figure 1: **(A)** Partially labeled plot of **1**. Hydrogen atoms, low occupancy disordered atoms, counter ions, and lattice solvent molecules were omitted for clarity. Color code: V, purple; O, red; N, blue; C, white.

(B) The coordination polygon of the title metal complex assembly. Hydrogen and low occupancy disordered atoms omitted for clarity.

(C) Lattice view with hydrogen bonding interactions in blue.

Figure 2: ESI-MS spectrum of **1**.

Figure 3: Solution ^{1}H (**A**) and ^{13}C-NMR (**B**) spectra of **1** in DMSO-d_6. The peaks marked as S are due to the solvent.

Figure 4: UV-Visible spectra of **1** (black line) and pure QC (red line).

Figure 5: Fluorescence excitation and emission spectra of **1** (red line) and pure QC (black line).

Figure 6: **A**) TGA diagram of **1**, and **B**) XRD pattern of the TGA residue (CeO_2).

Figure 7: The total density of states (DOS) of Ce-quercetin complex, and the projected density of states from individual contributions of Ce, C, N, and O atoms. The Fermi level is shifted to 0 eV.

Figure 8: The partial charge density diagram of the Ce-quercetin complex for the closest band below (a) and above (b) the Fermi level. Isosurface level was set to 0.002.

Figure 9: Growth inhibition of baker's yeast cells, grown in MMS medium for 24 h with several concentrations (2, 4, 6, 8, 10, and 20 μM) of compound **1** (red bars), QC (green bars), Ce(III) (blue bars), or phen (pink bars). Growth has been estimated after measuring culture turbidity (A_{600}). Compound **1** and phen significantly hindered growth of yeast cells with increasing concentrations, with the effect of studied concentrations of QC and Ce(III) not being significant. Statistical significance compared to control: $p>0.05$ (ns), $p<0.05$ (*), $p<0.01$ (**) and $p<0.001$(***).

Figure 10: Yeast cells viability in the presence of various concentrations (2, 4, 6, 8, 10, and 20 μM) of compound **1** compared to control, as estimated by the enzymatic hydrolysis of FDA for 30 min at 30 ^{o}C (**A**). The fluorescence of the hydrolyzed product has been measured after excitation at 494 nm and emission at wavelengths between 500-560 nm, with a peak at about 523 nm (**B**). Results prove that compound **1** significantly disturbs yeast cells metabolic activity, as

reflected in decreased enzymatic hydrolysis. Statistical significance compared to control: $p>0.05$ (ns), $p<0.05$ (*), $p<0.01$ (**) and $p<0.001$(***).

Figure 11: Agarose (1% w/v) gel electrophoresis of yeast DNA isolated from cells incubated with compound **1** for 24 h. Each sample containing the same DNA quantity; Lane L: 1 kb ladder. Lanes 1-7: DNA isolated from yeast cells treated with 0, 2, 4, 6, 8, 10 and 20 μM of compound **1**. Two main bands were visualized. The higher, less motile band, increases in intensity as the concentration of **1** increases, whereas the lower band intensity decreases, pointing toward possible aggregation of DNA under the effect of **1** or DNA binding ability of **1**.

Figure 12: Levels (% of control) of free ROS in yeast cells. Cells were grown in the presence of several concentrations (2, 4, 6, 8, 10 and 20 μM) of compound **1** (red bars), QC (green bars), Ce(III) (blue bars), or phen (pink bars) and incubated in the presence of 1 mg/mL NBT for 30 min. After the reaction, the formazan product was dissolved in DMSO and the absorbance was measured at 575 nm. Free ROS increased significantly in the presence of different concentrations of the Ce-complex, with a significant drop of their levels documented in cells incubated with QC, Ce(III), and phen alone. For all samples analyses, p value versus the control sample was <0.001.

Figure 13: Levels (% of control) of MDA in yeast cells cultures. Cells were grown in the presence of several concentrations (2, 4, 6, 8, 10 and 20 μM) of compound **1** (red bars), QC (green bars), Ce(III) (blue bars), or phen (pink bars) and incubated in the presence of TBA reagent solution [0.188g of TBA in 50 mL of 0.25 N HCl, 10% (w/v) TCA] for 1 h, at 95 ^{o}C. After the reaction, the TBA-MDA product was measured at 532 nm, against a blank containing 0.25 N HCl, and 10% (w/v) TCA. MDA increased significantly in the presence of different concentrations of all studied compounds, especially under the influence of **1** and phen. Statistical significance compared to control: $p>0.05$ (ns), $p<0.05$ (*), $p<0.01$ (**) and $p<0.001$(***).

Figure 14: Inhibition of stable free radical DPPH• in the presence of several concentrations of either compound **1** (black rectangles) or QC (red circles). Both compounds exhibit scavenging properties, with **1** proven to be more efficient than QC (IC_{50} = 5.8 ± 1 μM, and 10.7 ± 1 μM, respectively).

Figure 15: Antibacterial ability of several quantities (25, 50, 75 and 100 μg) of compound **1** or QC on *E. coli* (**A**), *S. aureus* (**B**), and *B. cereus* (**C**) LB agar cultures, based on the well-diffusion method. Inhibition of bacterial growth is given as the diameter (cm) of the clear zone around the wells. Kanamycin (Km) was employed as a positive control. An indicative plate (**D**) is given for *S. aureus* growth in the presence of 25, 50 and 100 μg of **1** and 100 μg of Km. Clear zones, with no bacterial colonies, are visible around the wells. Statistical significance compared to control: $p>0.05$ (ns), $p<0.05$ (*), $p<0.01$ (**) and $p<0.001$(***).

Figure 16: Binding pose architecture of compound **1** in the crystal structure of *Saccharomyces Cerevisiae* DNA (PDB accession no. 1YTF) depicting its stabilization in the binding cavity of minor groove (upper left panel). A docking pose from a view above the axis of the helix (shown by a 90-degree rotated view of the structure) to illustrate the extent of insertion of docked molecule in the interior of double strand DNA, is also illustrated (upper right panel). DNA structure is depicted as semitransparent surface and cartoon representation, in deep teal and deep purple (clones A and B, respectively). A close-up stereo view (cross-eye) of the ligand-binding site illustrating the binding interactions of **1** is also depicted (lower part). DNA structure is illustrated as cartoon, while base pair nucleotides are rendered in line representation and color-coded by atom type according to DNA strand color. Dotted lines in split pea green indicate hydrogen bond, polar, π-π stacking, pi-polar type, and pi-alkyl type interactions, between the docked molecule and the nucleotides in the binding pocket of DNA. Docked molecule is rendered either in stick (upper panel) or ball-and-stick (lower panel) mode and colored according to atom type in yellow orange C atoms. Heteroatom color-code: O: red, N: blue, and Ce: white. Hydrogen atoms are omitted from all molecules for clarity. Nucleotides are numbered according to PyMol software. The final structure was ray-traced and illustrated with the aid of PyMol Molecular Graphics System.

Figure 17: Binding pose architecture of QC and phen in the crystal structure of *Saccharomyces Cerevisiae* DNA (PDB accession no. 1YTF) depicting their stabilization in the binding cavity of minor groove (left panel). A docking pose from a view above the axis of the helix (shown by a 90-degree rotated view of the structure) to illustrate the extent of insertion of docked molecules in the

interior of double strand DNA, is also illustrated (right panel). DNA structure is depicted as semitransparent surface and cartoon representation, in deep teal and deep purple (clones A and B, respectively). Docked molecules are rendered in ball-and-stick mode and colored according to atom type in white and limon C atoms for QC and phen, respectively. Heteroatom color-code: O: red and N: blue. Dockings of both ligands were performed individually. Hydrogen atoms are omitted from all molecules for clarity. The final structure was ray-traced and illustrated with the aid of PyMol Molecular Graphics System.

Figure 18: Docking pose orientation of compound **1** (rendered in stick mode and colored according to atom type in yellow C atoms) superimposed with the co-crystallized drug CBN (hot pink C atoms rendered in stick representation) on DNA-gyrase (PDB ID: 1kzn) (upper panel). Target protein is illustrated as cartoon with additional depiction of semitransparent surface colored according to chain in split pea green with depth cue in the ray-tracing rendering of the cartoon. The ligand-binding site of the molecules depicting the extent of the pocket as determined by the computation process labeling the critical amino acid residues interacting with both molecules is shown in the lower panel. Selected contacting residues of the binding pocket are rendered in stick model and colored in deep purple. Heteroatom color-code: O: red, N: blue, Ce: white. Binding contacts are shown as white dotted lines. Hydrogen atoms are omitted for clarity. The final structure was ray-traced and illustrated with the aid of PyMol Molecular Graphics.

Figure 19: Binding pose architecture of compound **1**, QC, and phen superimposed with the co-crystallized ligand GSH (hot pink C atoms rendered in ball-and-stick representation) in the crystal structure of yeast *s. cerevisiae* glutathione S-transferase (PDB ID: 3IBH) (upper panel). Target protein is illustrated as cartoon with additional depiction of semitransparent surface colored according to chain in chocolate color with depth cue in the ray-tracing rendering of the cartoon. Docked molecules are rendered in ball-and-stick mode and colored according to atom type in yellow-orange, white, and marine blue C atoms for compound **1**, QC, and phen, respectively. The ligand-binding site of the molecules depicting the extent of the pocket as determined by the computation process labeling the critical amino acid residues interacting with both molecules is shown in the lower panel. Selected contacting residues of the binding pocket

are rendered in stick model and colored according to cartoon color. Heteroatom color-code: O: red, N: blue, S: yellow, and Ce: white. Binding contacts of compound **1** and GSH are shown as white and yellow dotted lines, respectively. Interactions between GSH and compound **1** are indicated by teal dotted lines. Hydrogen atoms are omitted for clarity. The final structure was ray-traced and illustrated with the aid of PyMol Molecular Graphics.

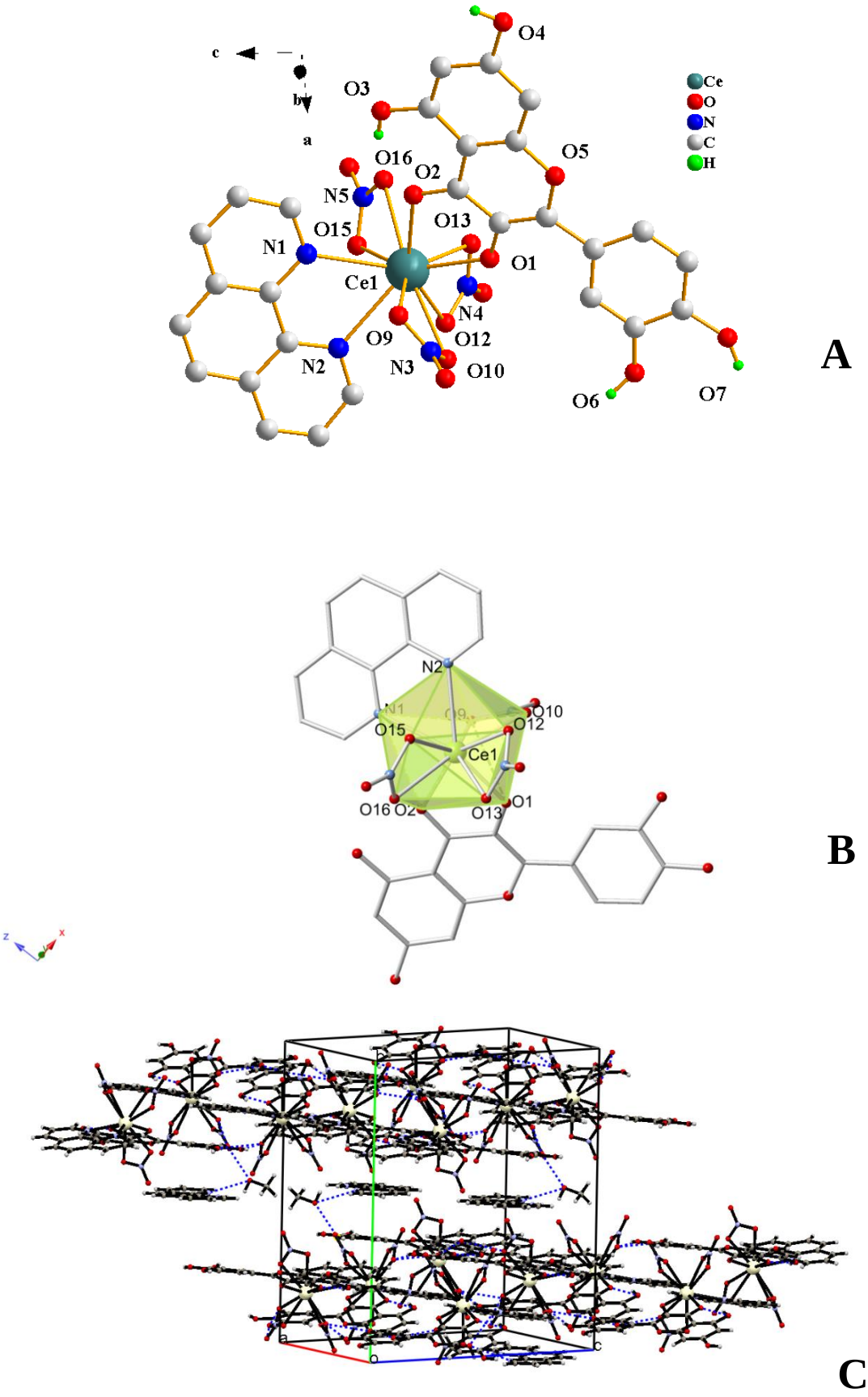
c
b
a
O4
O3
O16
O2
O5
N5
O15
O13
N1
O1
Ce1
N4
O9
O12
N2
N3
O10
O6
O7
Ce
O
N
C
H
A
N2
N1
O9
O10
O12
O15
Ce1
O16
O2
O13
O1
B
z
x
C

Figure 1

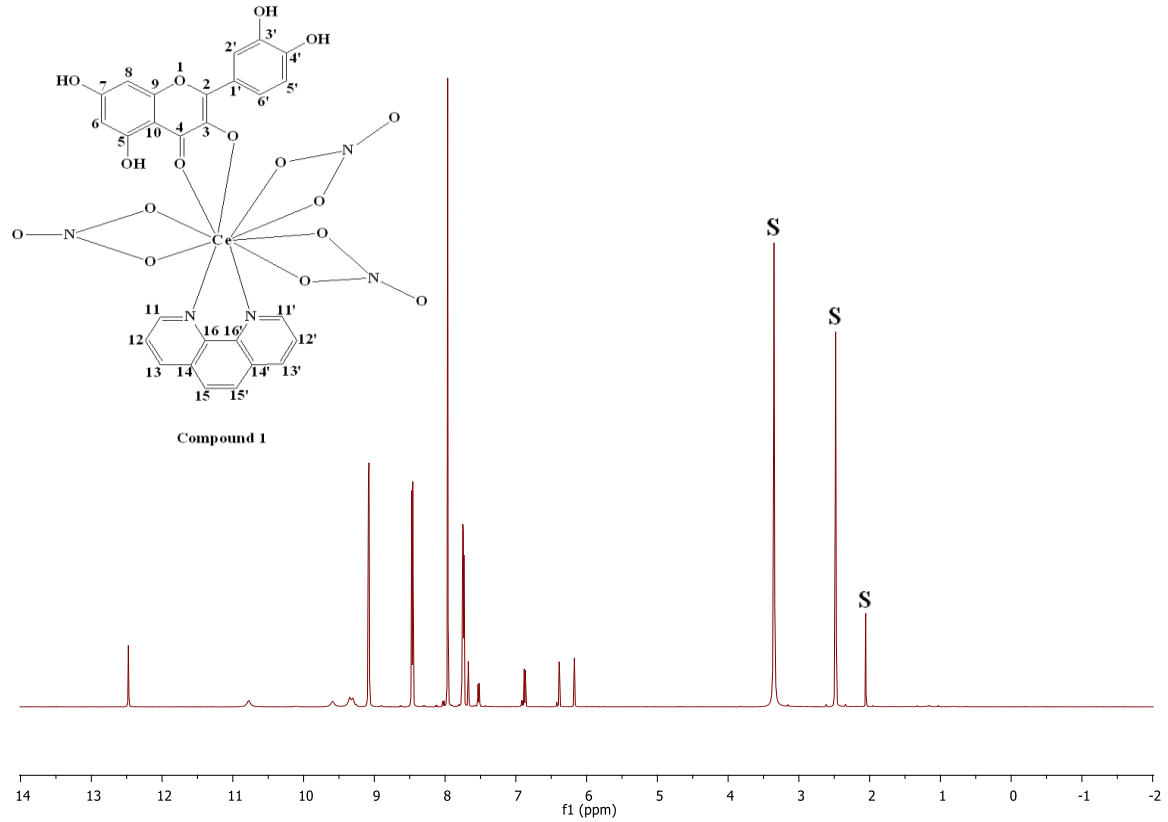

A

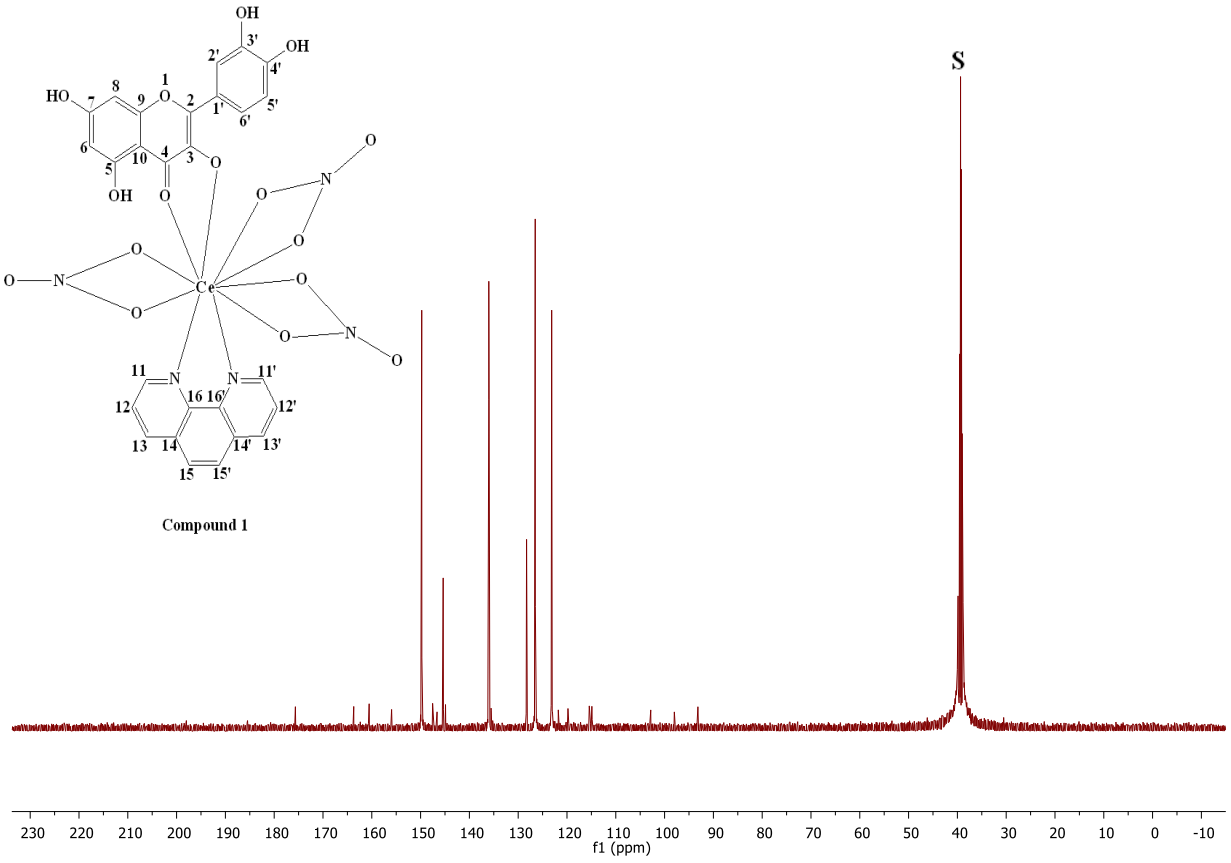

B

Figure 3

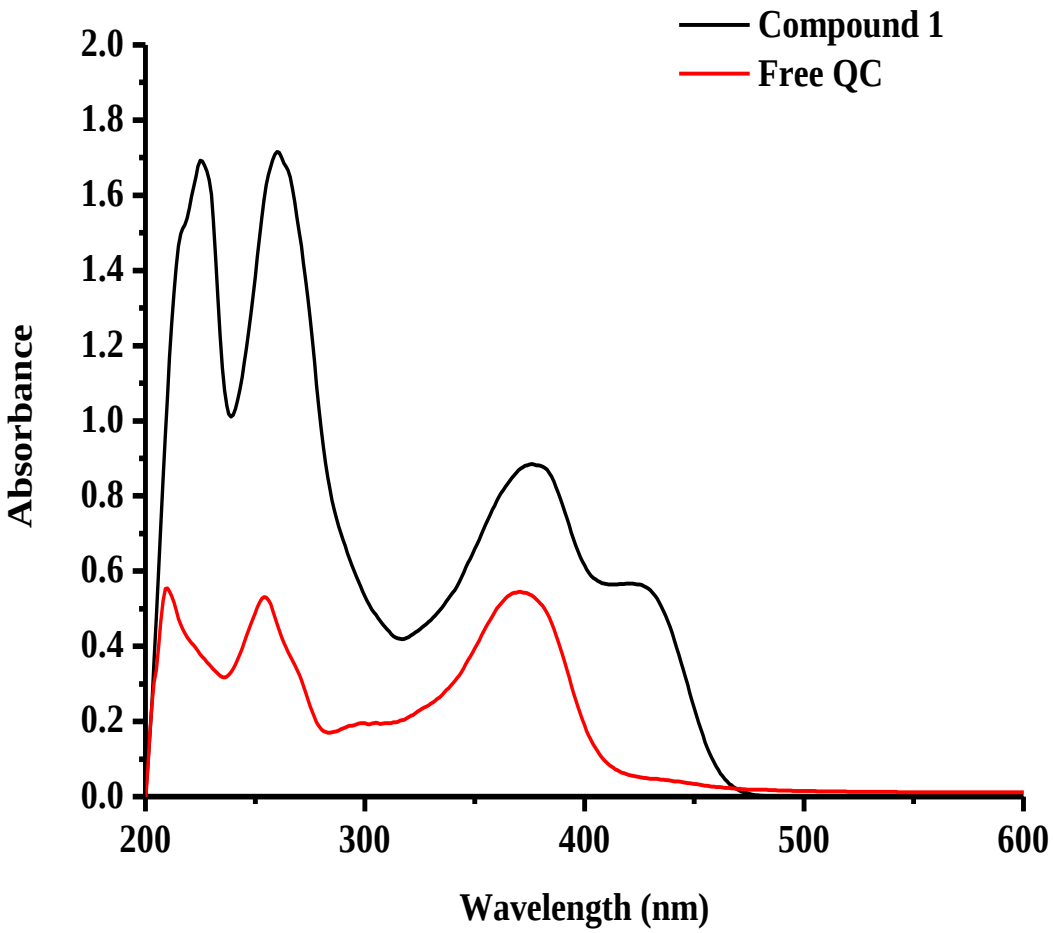
Compound 1
Free QC
Absorbance
2.0
1.8
1.6
1.4
1.2
1.0
0.8
0.6
0.4
0.2
0.0
200
300
400
500
600
Wavelength (nm)

Figure 4

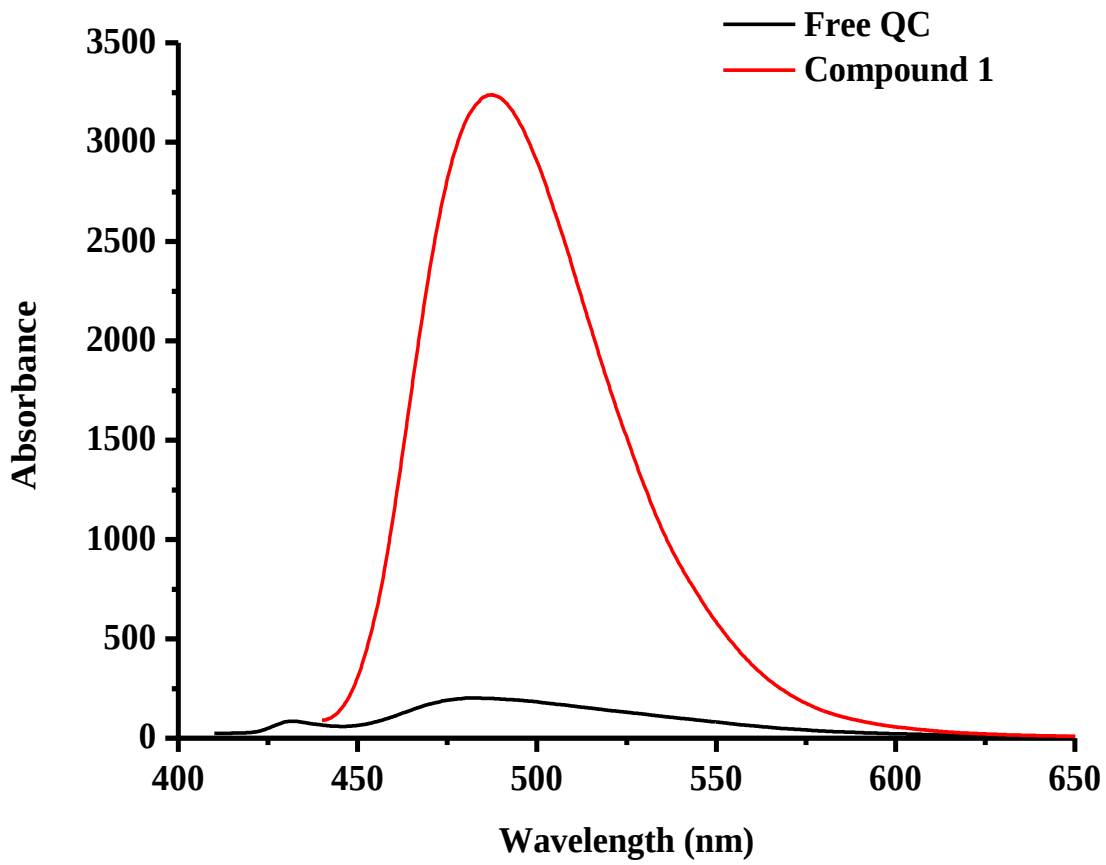
Free QC
Compound 1
Absorbance
3500
3000
2500
2000
1500
1000
500
0
400
450
500
550
600
650
Wavelength (nm)

Figure 5

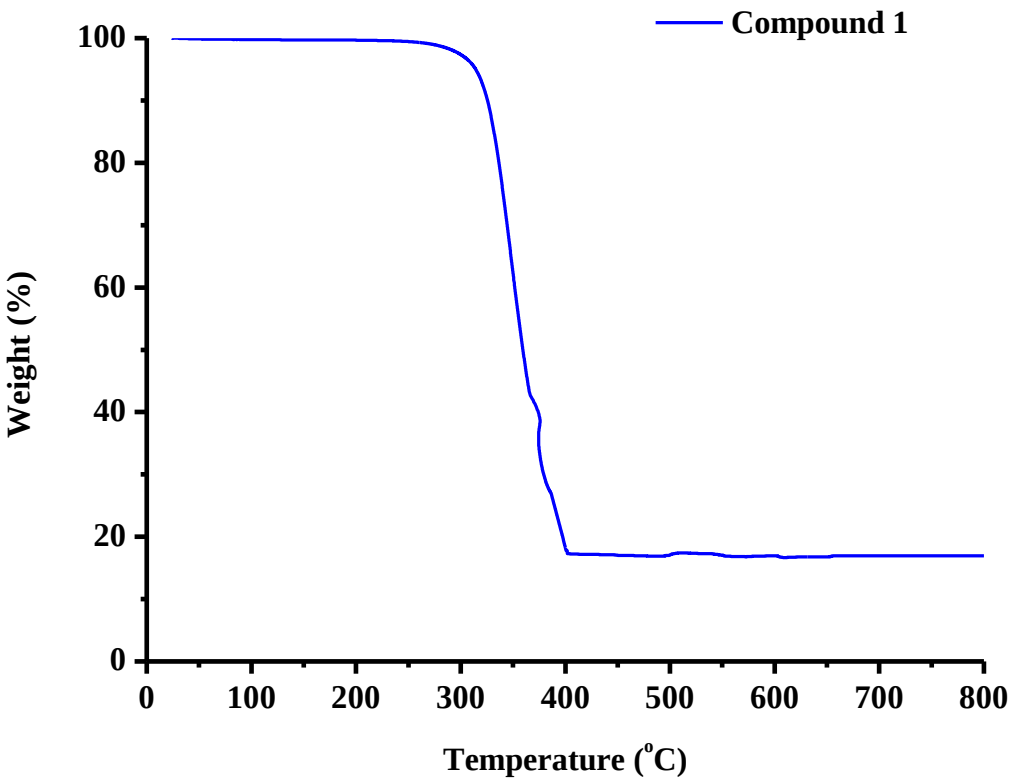
Compound 1
Weight (%)
100
80
60
40
20
0
0
100
200
300
400
500
600
700
800
Temperature (°C)

A

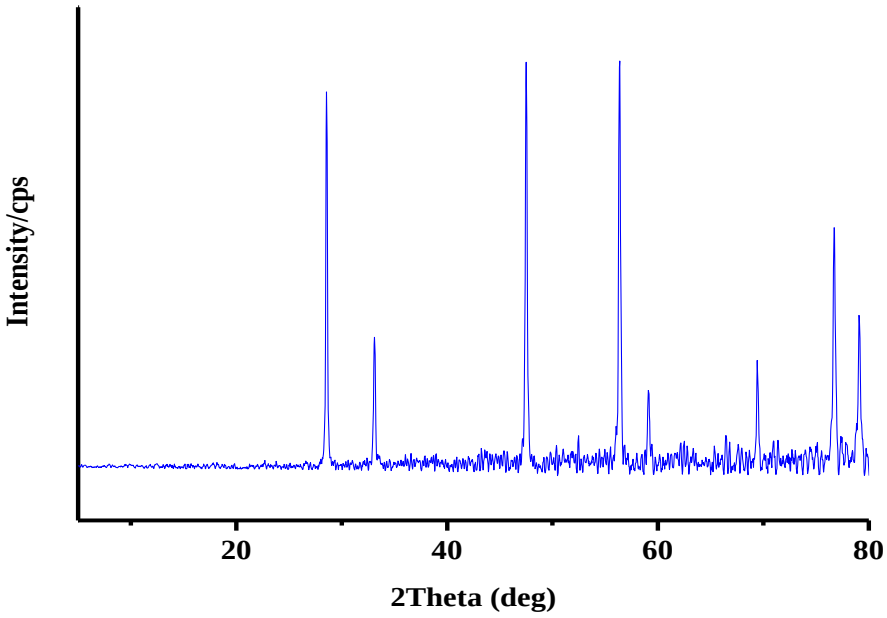
Intensity/cps
20
40
60
80
2Theta (deg)

B

Figure 6

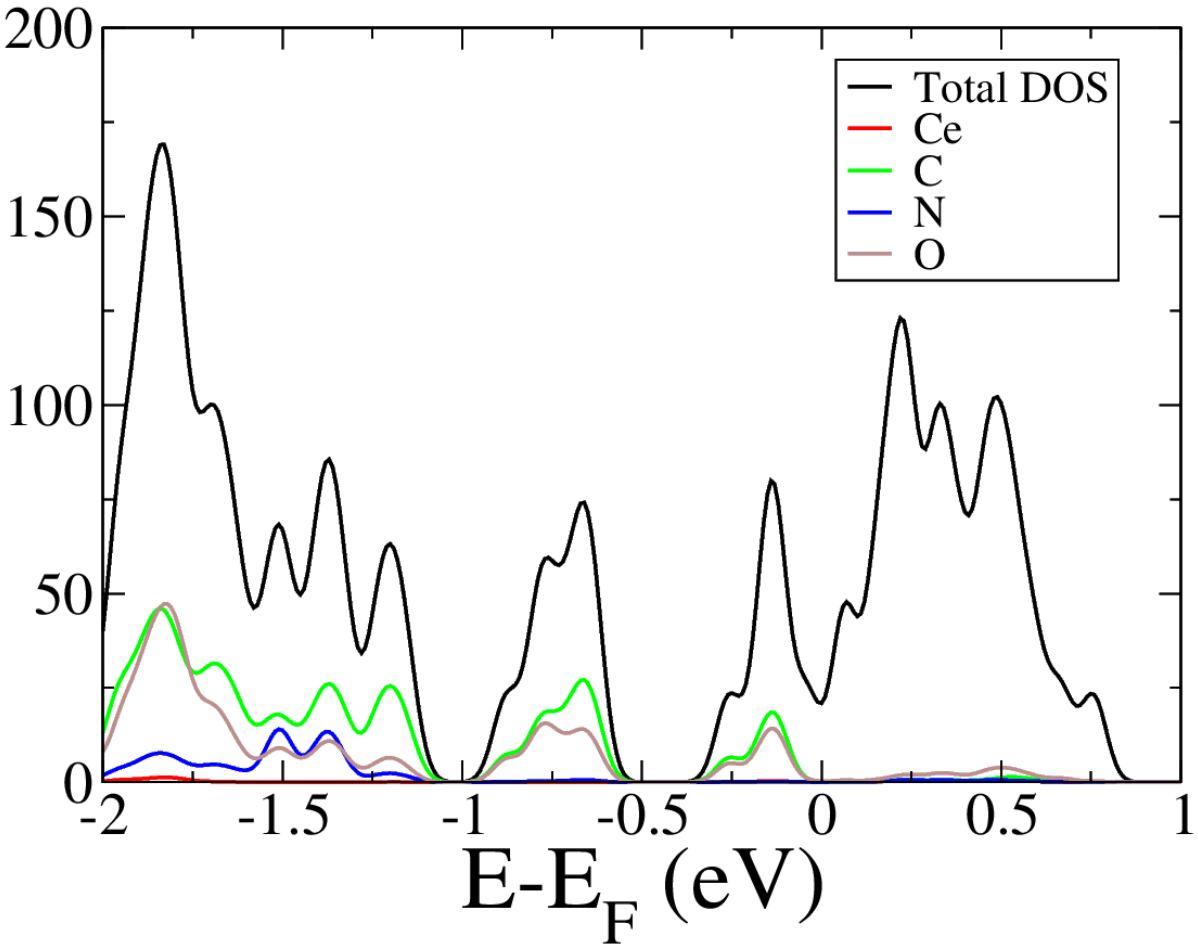

Figure 7

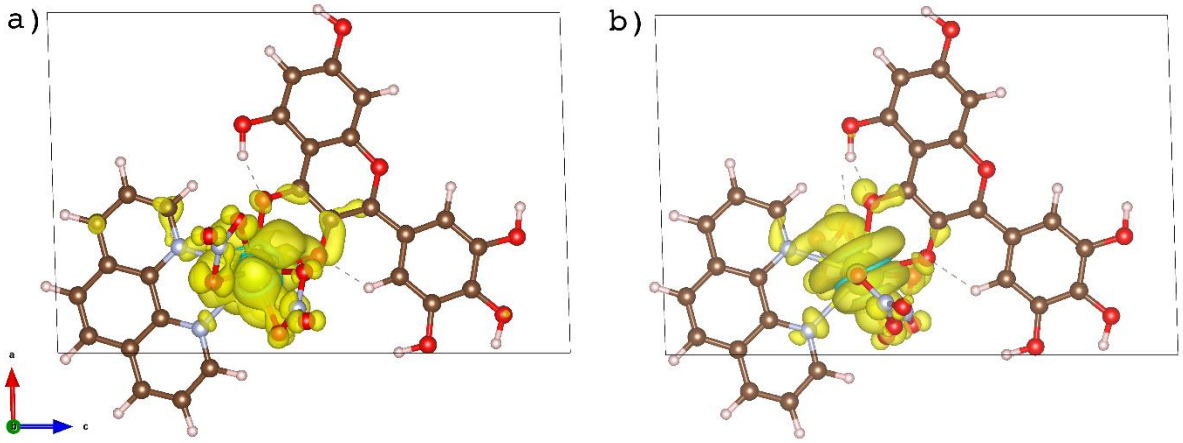

Figure 8

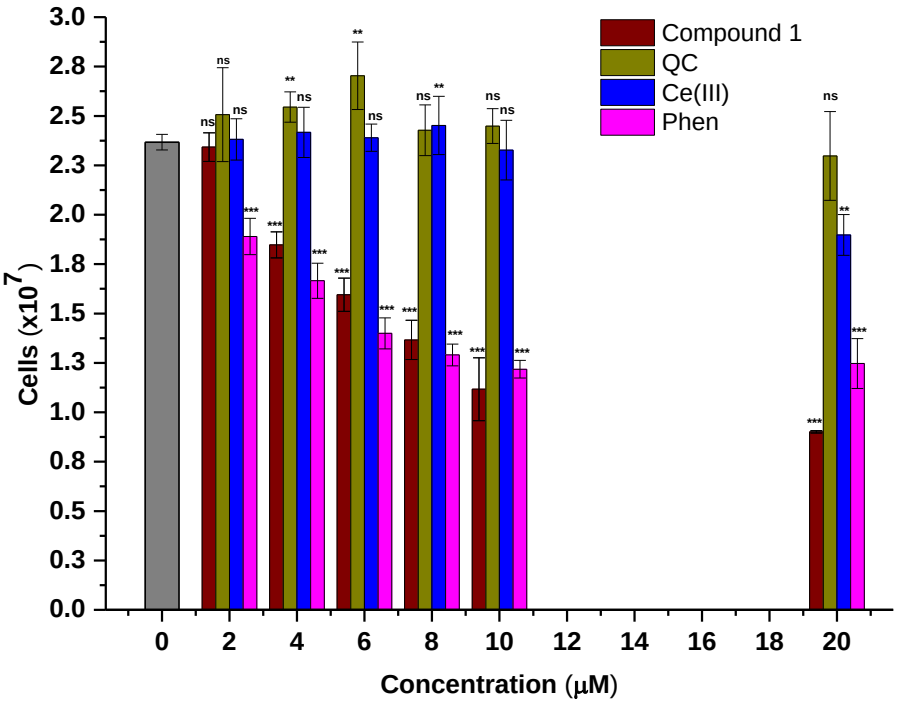

Figure 9

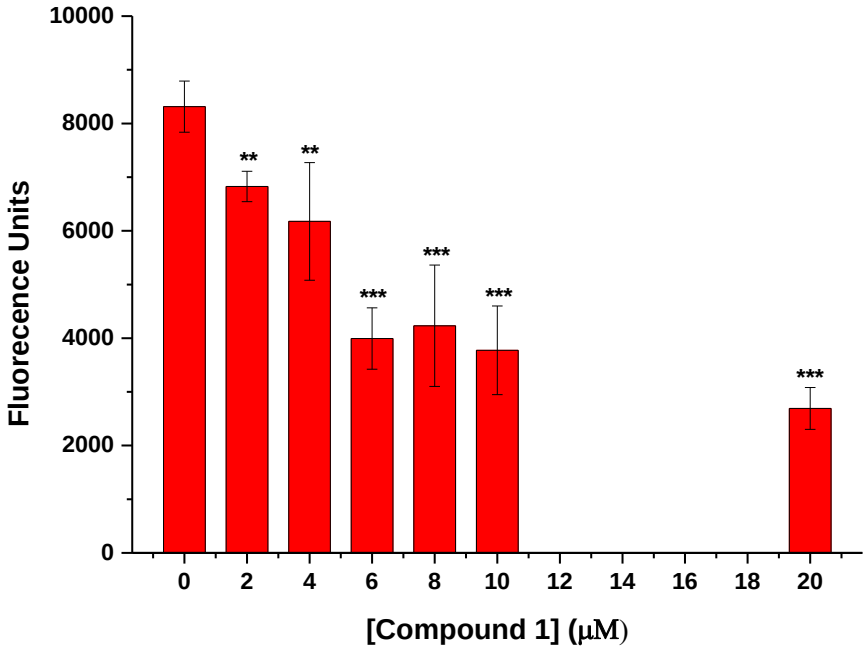

Figure 10

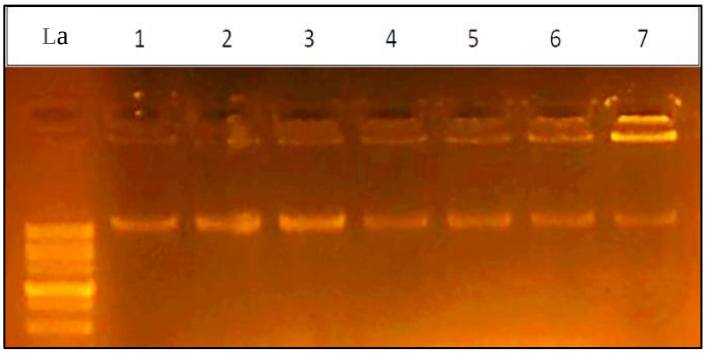

Figure 11

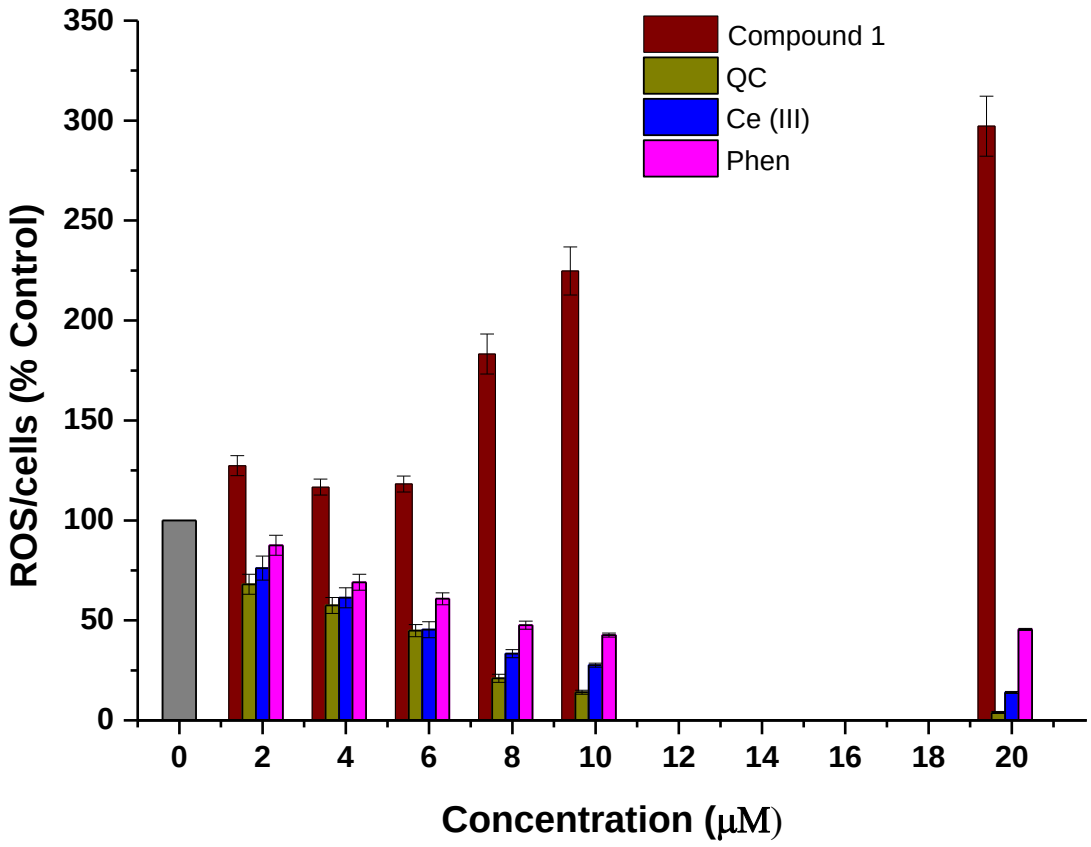
Compound 1
QC
Ce (III)
Phen
ROS/cells (% Control)
350
300
250
200
150
100
50
0
0
2
4
6
8
10
12
14
16
18
20
Concentration (μM)

Figure 12

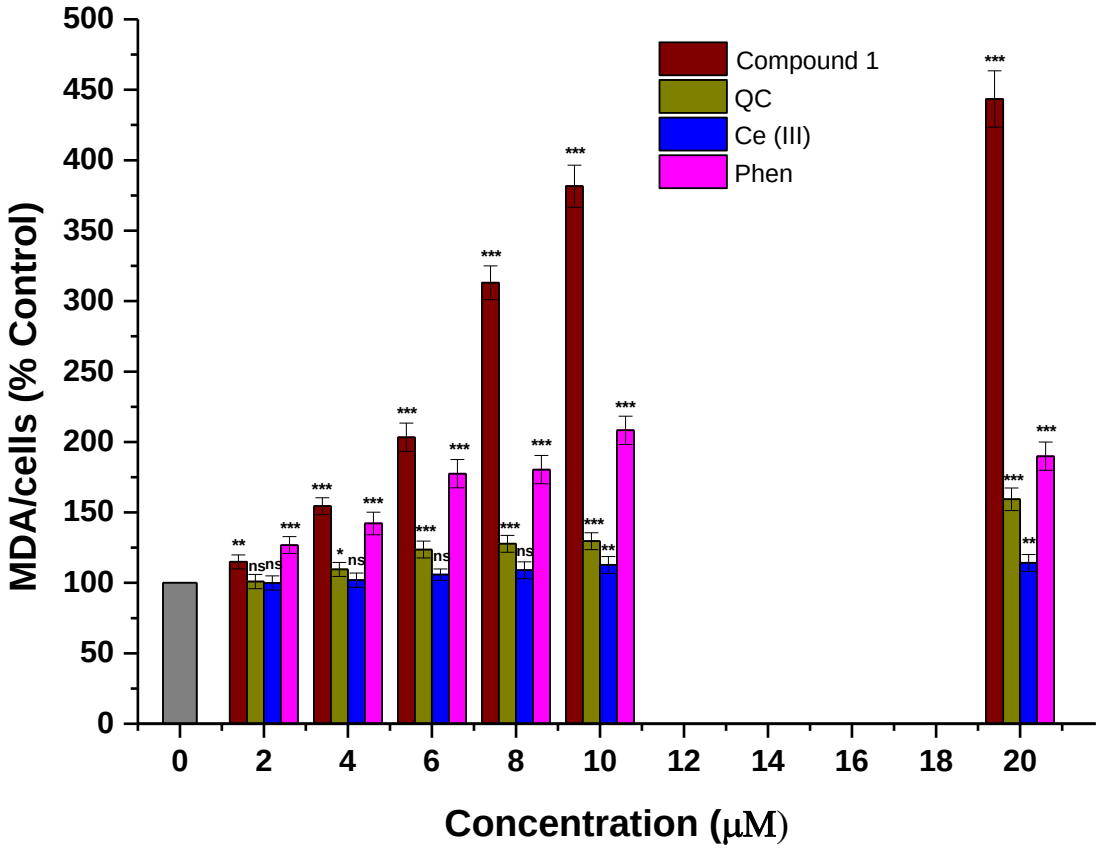
MDA/cells (% Control)
Concentration (μM)
Compound 1
QC
Ce (III)
Phen
0
50
100
150
200
250
300
350
400
450
500
0
2
4
6
8
10
12
14
16
18
20

Figure 13

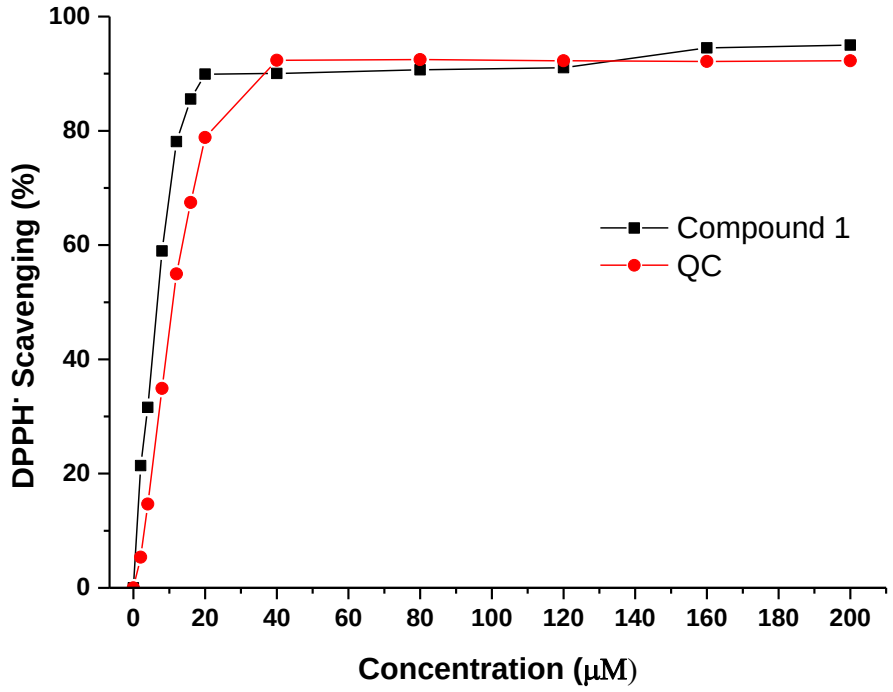
100
80
60
40
20
0
DPPH· Scavenging (%)
0
20
40
60
80
100
120
140
160
180
200
Concentration (μM)
Compound 1
QC

Figure 14

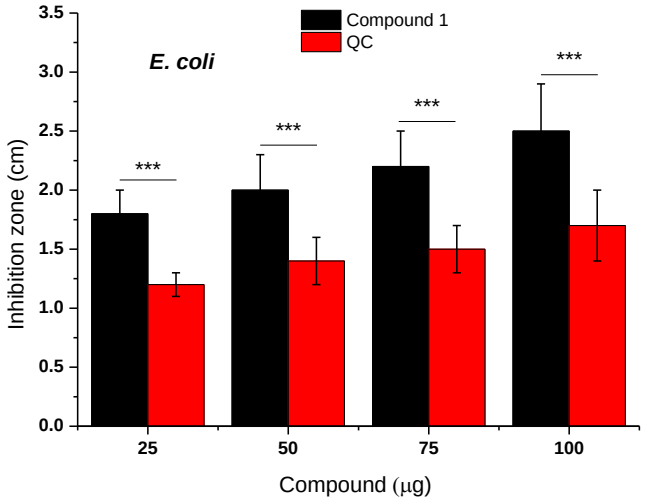

A

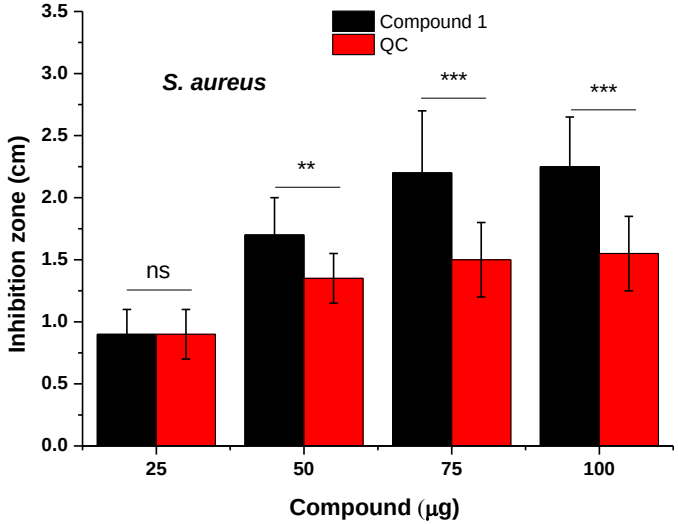

B

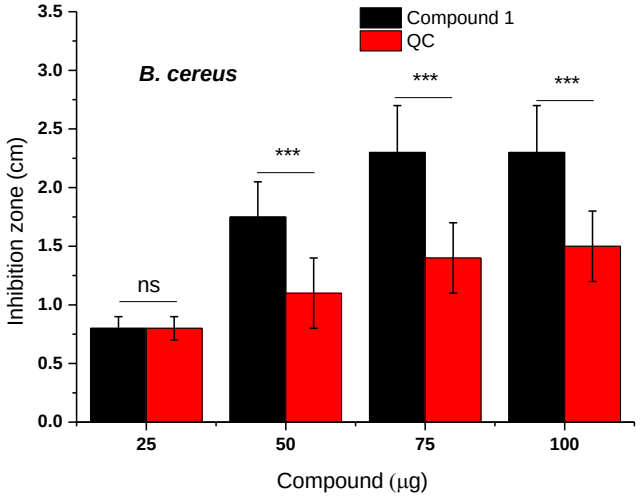

C

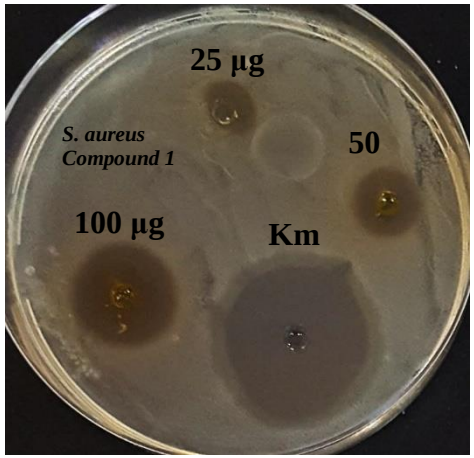

D

Figure 15

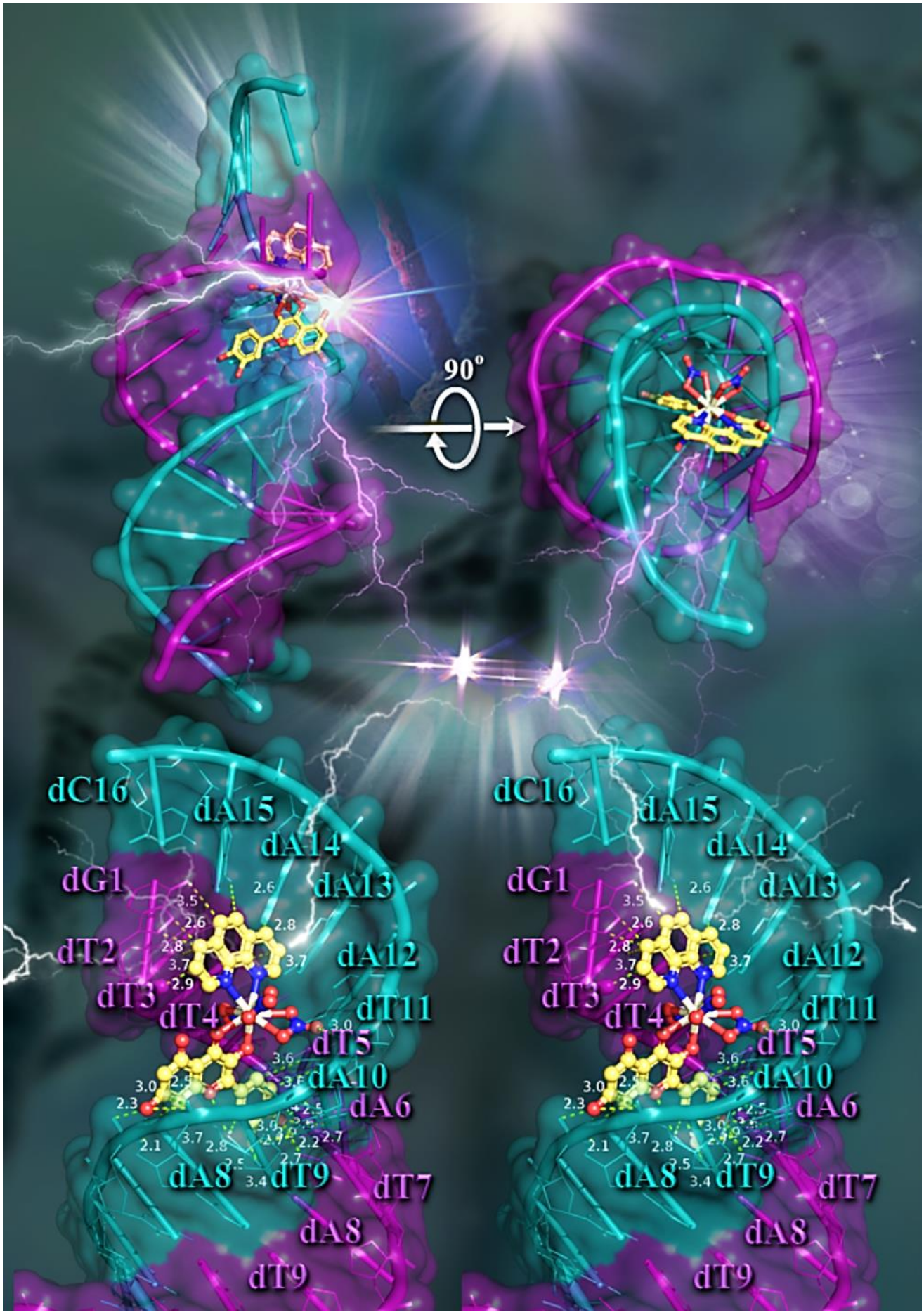
90°
dC16
dA15
dA14
dG1
dA13
dT2
dA12
dT3
dT4
dT11
dT5
dA10
dA6
dA8
dT9
dT7
dA8
dT9
dC16
dA15
dA14
dG1
dA13
dT2
dA12
dT3
dT4
dT11
dT5
dA10
dA6
dA8
dT9
dT7
dA8
dT9

Figure 16

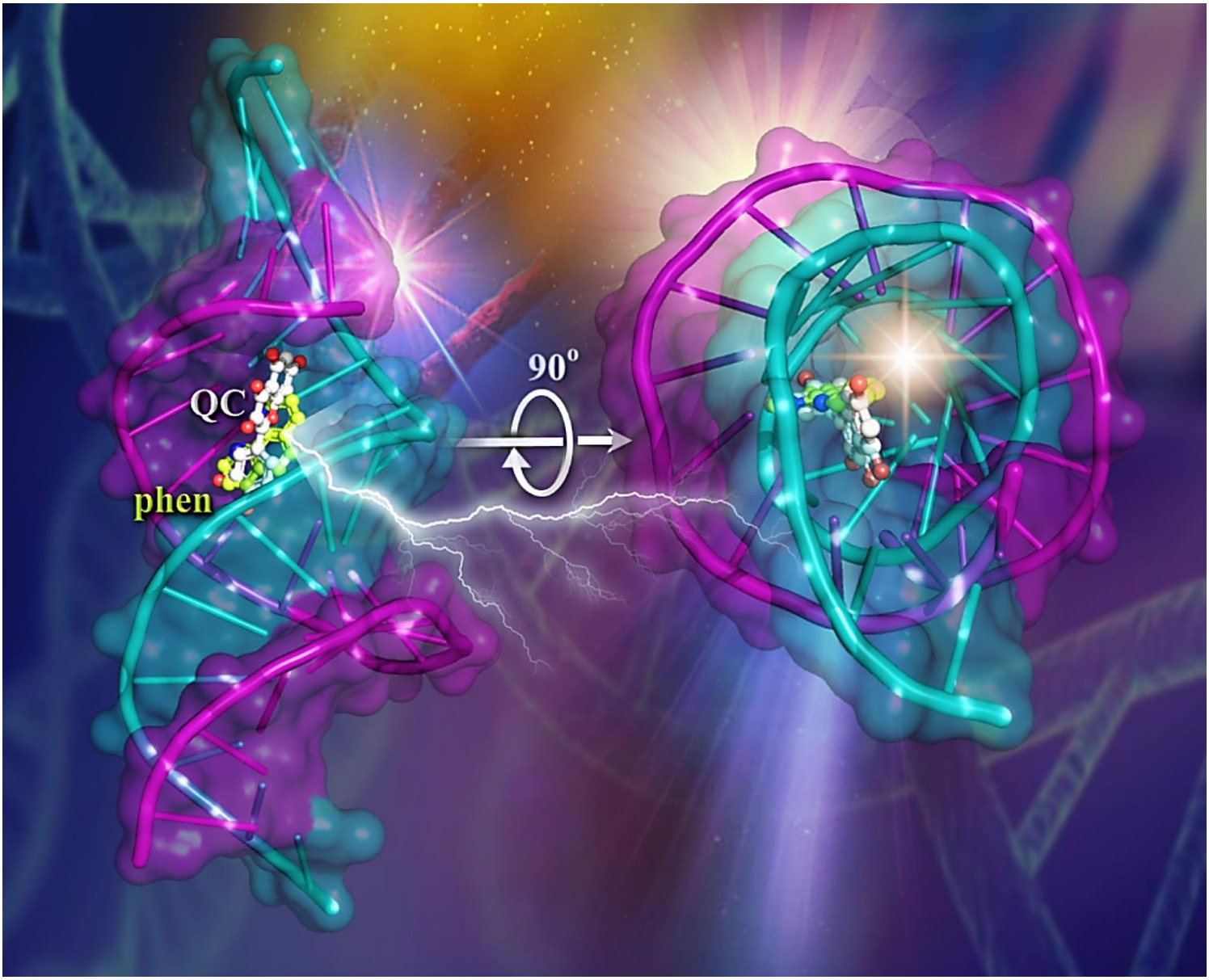

Figure 17

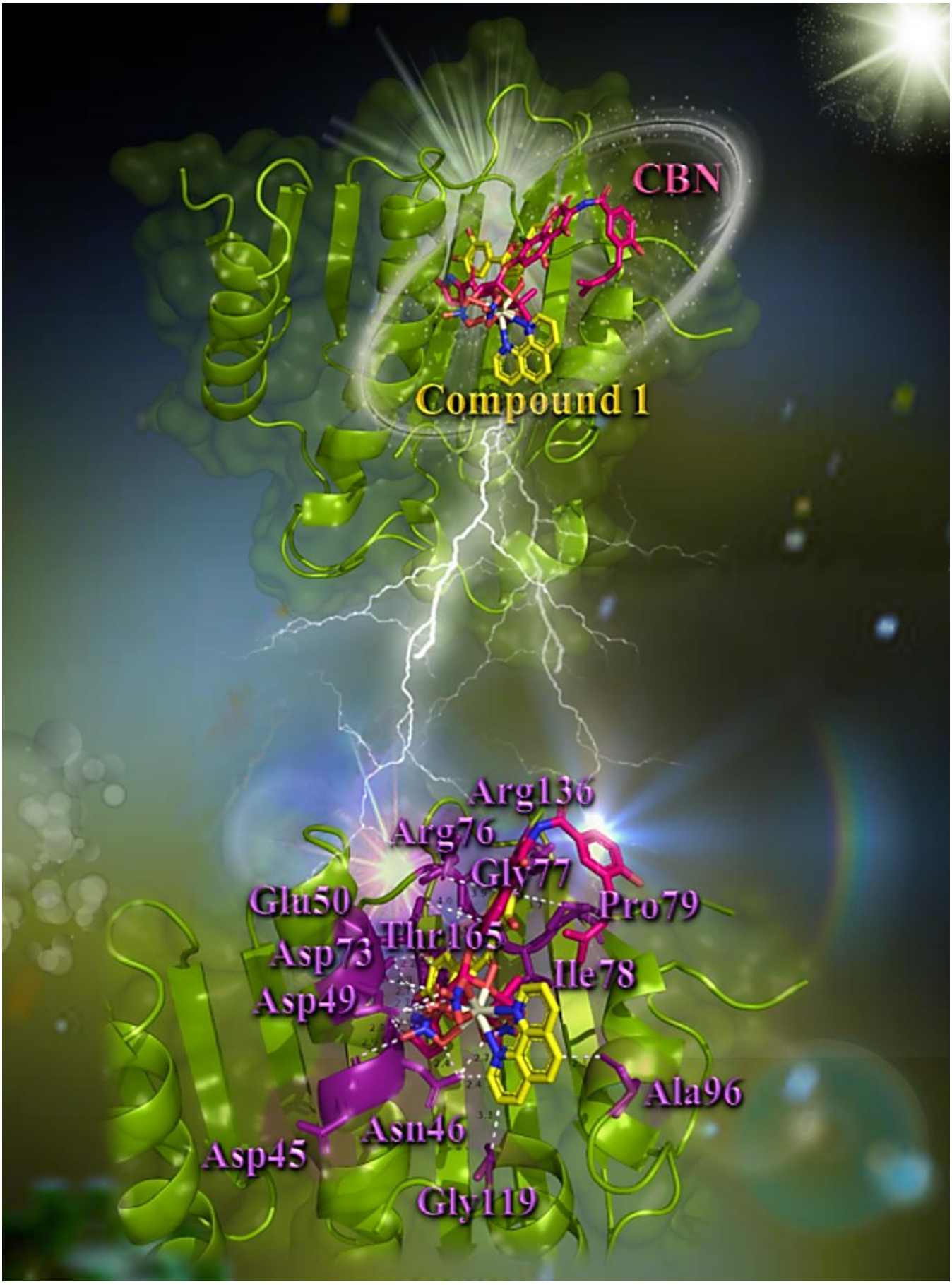
CBN
Compound 1
Arg136
Arg76
Gly77
Glu50
Pro79
Thr165
Asp73
Ile78
Asp49
Ala96
Asn46
Asp45
Gly119

Figure 18